# UC San Diego

## UC San Diego Electronic Theses and Dissertations

**Title**

Computational and Experimental Techniques for Expanding the Applicability of Cryo-Electron Tomography to Cell Biology

**Permalink**

https://escholarship.org/uc/item/60s0m1kp

**Author**

Croxford, Matthew

**Publication Date**

2022

**Supplemental Material**

https://escholarship.org/uc/item/60s0m1kp#supplemental

Peer reviewed|Thesis/dissertation

UNIVERSITY OF CALIFORNIA SAN DIEGO

Computational and Experimental Techniques for Expanding the Applicability of Cryo-Electron
Tomography to Cell Biology

A dissertation submitted in partial satisfaction of the
requirements for the degree Doctor of Philosophy

in

Biology

by

Matthew Croxford

Committee in charge:

       Professor Elizabeth Villa, Chair
       Professor Arshad Desai
       Professor Nan Hao
       Professor Padmini Rangamani
       Professor James Wilhelm

2022

The Dissertation of Matthew Croxford is approved, and it is acceptable in quality and form for publication on microfilm and electronically.

University of California San Diego

2022

TABLE OF CONTENTS

LIST OF FIGURES

# LIST OF SUPPLEMENTAL FILES

ACKNOWLEDGEMENTS

I would like to acknowledge Professor Elizabeth Villa for her support and mentorship as the chair of my committee.

I would also like to acknowledge John Sedat of UC San Francisco, who was my primary collaborator and unofficial co-mentor.

Chapter 2, in full, is a reprint of the material as it appears in Matthew Croxford, Michael Elbaum, Muthuvel Arigovindan, Zvi Kam, David Agard, Elizabeth Villa, John Sedat, "Entropy-regularized deconvolution of cellular cryotransmission electron tomograms," Procedings of the National Academy of Sciences 2021. I performed all new work on this manuscript with input from other authors. John Sedat and Elizabeth Villa directed and supervised the research which forms the basis for this chapter.

Chapter 3 details unpublished work documenting a project that ultimately led to negative results. The device detailed in this chapter will be described in a future publication. I was the primary investigator and author of this chapter. Initial work on the device was done by Vinson Lam, who began the project as part of a rotation in the qBio specialization program.

Chapter 4 details progress on an ongoing project in the lab in collaboration with Josh Hutchings, who will continue the project for future publication.

## VITA

| | |
|---|---|
| 2014 | Bachelor of Science, Western Washington University |
| 2022 | Doctor of Philosophy, University of California San Diego |

## PUBLICATIONS

"Entropy Regularized Deconvolution of Cellular Cryo-Transmission Electron Tomograms" Proceedings of the National Academy of Sciences of the United States of America, vol. 118, issue 50, December 2021

ABSTRACT OF THE DISSERTATION


Computational and Experimental Techniques for Expanding the Applicability of Cryo-Electron
Tomography to Cell Biology


by


Matthew Croxford


Doctor of Philosophy in Biology


University of California San Diego, 2022


Professor Elizabeth Villa, Chair


The field of cell biology originated with, and has always been inextricably tied to, the microscope. Direct visualization has always been a key technique for understanding cell organization and behavior. Today, cell biologists have microscopes many orders of magnitude more powerful than their progenitors, enabling the direct visualization of cells and their constituent parts down to sub-nanometer resolution. Cryo-focused ion beam milling combined with cryo-elecyron tomography (cryo-FIB-ET) is a technique in which cells are rapidly frozen to preserve them in their native state, followed by focused ion beam (FIB) thinning of the frozen cells, which allows for the collection of high resolution transmission electron microscopy data. When these

electron micrographs are collected over a range of different tilt angles, a full three-dimensional reconstruction of the cellular interior can be made and analyzed. However, despite the un-precedented level of detail available to cell biologists through cryo-FIB-ET, several challenges hinder its applicability to cell biology. On the experimental side, commonly used cryo-FIB-ET compatible substrates were not designed with cell biology in mind, and have features that make them sub-optimal for this purpose. Furthermore, limitations in the range of tilts at which data may be collected lead to missing information in the three-dimensional reconstructions that cause distortions and make the resulting volumes more difficult to interpret. The work presented in this dissertation focuses on both of these issues in an attempt to increase the utility of cryo-FIB-ET for cell biologists and expand the range of questions that may be addressed with the technique.

# Chapter 1

# Introduction

Recent advances in cryo-electron tomography (cryo-ET), most notably the ability to thin cryo-preserved specimens using a focused ion beam (FIB), have opened windows for the direct visualization of the cell interior at sub-nanometer-scale resolution [1, 2, 3, 4, 5, 6, 7, 8, 9]. Cells are rapidly frozen to achieve a vitreous form of ice that preserves biological molecules in a near-native state. They are then cryo-FIB milled to a suitable thickness of 100-350 nm for imaging with transmission electron microscopy (TEM). A series of projection images is acquired, typically with 1-5 degree increments and then reconstructed into a 3D volume [10]. This 3D reconstruction is rendered for display and analysis, which may entail segmentation to highlight extended structures or averaging of sub-volumes for enhancement of molecular-scale resolution [11, 12, 13]. However, despite these recent advances in the field, a number of challenges remain.

First, the process of cryo-ET requires samples to be imaged over a range of different tilts for several reasons. For one, the sample is held on the microscope stage in a metal holder, meaning that a sample tilted 90° will block the electron beam entirely due to holder. Related to this, a sample's effective thickness increases with the tilt angle with the relationship of $thickness * \frac{1}{cos(\theta)}$. With this increasing thickness comes increased inelastic scattering of electrons through the sample, steadily reducing the signal to noise ratio of the resulting data [14]. In addition to the increased thickness as the tilt series progresses, the sample also accumulates

1

radiation damage, reducing high frequency information in later tilts and eventually burning the sample entirely [15]. These factors mean that tilt series are typically limited from -60° to +60°. The inability to sample all angles leads to serious anisotropic distortions in the resulting tomograms along the axis of the electron beam.

Another challenge is that in order to perform cryo-ET on cells, they must be grown or deposited on standardized substrates that are compatible with the multiple different microscopes necessary for cellular electron tomography. The traditional substrates used for cryo-ET were originally developed for single-particle cryo-EM, where one takes micrographs of many copies of the same biological macromolecule in solution. Thus, an EM compatible platform more closely resembling traditional cell biology substrates (e.g. glass, polystyrene) would greatly expand the range of questions answerable through cryo-ET.

Here I describe efforts to address some of these issues with sample preparation and data distortions. In chapter two I will describe our efforts to ameliorate the anisotropic distortions in reconstructed tomograms by applying a deconvolution algorithm designed for data with a low signal to noise ratio to cryo-electron tomograms, and subsequent analyses of the algorithm's performance. In chapter three I will describe our efforts to characterize silicon nitride (SiN) as a potential alternative platform for cryo-FIB-ET. Specifically, I address issues such as on grid cell culture, sample drying, as well as the drawbacks of SiN with respect to cryo-FIB milling. Together, these efforts will hopefully aid in the continued expansion of cryo-FIB-ET as an unparalleled tool for high resolution structural cell biology.

# Chapter 2

# Entropy Regularized Deconvolution of Cellular Cryo-Transmission Electron Tomograms

## 2.1  Introducton

While cryo-ET offers unparalleled resolution of cellular interiors, it is challenging for a number of reasons. First, vitrified biological samples are highly sensitive to damage by the electron irradiation required for imaging. Constraints on the permissible exposure result in limited contrast and a low signal to noise ratio [15]. Additionally, higher resolution information is degraded by radiation damage over the course of imaging [16], though approaches such as dose-symmetric acquisition have been developed to optimize recording of high frequencies [17]. Second, the modality of wide-field TEM depends on defocus to generate useful phase contrast, but with a non-trivial dependence on spatial frequency that is expressed in a contrast transfer function (CTF). Contrast is lost at low spatial frequencies and oscillates at high spatial frequencies, meaning that material density could be represented as intensity either darker or lighter than background [18, 19, 20]. Post-processing is applied to correct this representation in the image intensities. The correction is inherently approximate, and is especially challenging in tomography where the defocus varies across the field of view for tilted specimens [21]. Third, the available raw data are never sufficient to produce an unambiguous reconstruction. The tilt range is
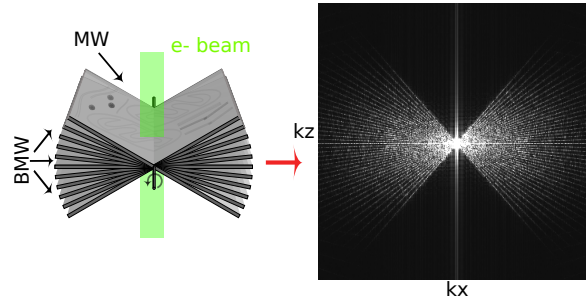
**Figure 2.1.** Left: Schematic of tilt-series collection scheme. Sample projections are acquired over a range of tilt angles, typically from -60° to +60° . Right: Middle slice of the kxkz plane shows the missing wedge (MW) and baby missing wedges (BMW) of information visualized in Fourier space. Attenuation of high frequencies due to radiation damage as tilt series progresses not depicted (see [16, 17]).

restricted by the slab geometry, typically to about 120° around the vertical. The projected thickness of a slab also increases with tilt angle, resulting in degraded contrast and resolution from these contributions to the reconstruction. The missing information is best recognized in Fourier space, where it is known as the missing wedge. The gaps between discrete tilt angles also leave small missing wedges as seen in Fig. 2.1. Since the reconstruction is equivalent to an inversion in Fourier space, it is obvious that some interpolation is required and that the data are incomplete. As such, it is not surprising that different algorithms can generate somewhat different reconstructions from the same data. Commonly recognized artifacts are elongation along the Z direction and streaks projecting from high contrast points into neighboring planes in the volume.

In addition to the missing wedges, TEM images require a significant defocus to get adequate contrast. For *in situ* cryo-ET data, a typical defocus of at least $5\,\mu$m is used. Finally, the process of reconstruction by weighted back projection (WBP) introduces well-known problems. These include significant intensity above and below the sample volume, where we expect vacuum with no signal. This is due to cross-terms in the WBP coming from the tilt wedges, as well as distortions in the WBP arising from the missing wedge. Because of these issues with cryo-ET data, filters to improve contrast and compensate for the missing wedge are an area of ongoing

research [22]. These techniques include non-linear anisotropic diffusion (NAD), convolutional neural networks based on detector noise models, wavelet based filtering methods, different implementations of deconvolution, and model based iterative reconstruction (MBIR) [23, 24, 25, 26, 27, 28, 29, 30, 31, 32]. Here, we present a deconvolution approach to achieve both enhanced SNR and missing wedge compensation.

The image distortions resulting from the incomplete tilt series and CTF can be characterized in terms of a single sample point in the data. This model is referred to as the point spread function (PSF), of which the hour-glass PSF in light microscopy is a classical example [33, 34, 35]. Formally, the PSF is convolved with all points in the specimen function to form what is recorded in the image [36]. If the PSF is well defined, it becomes possible to partially reverse the process of convolution to obtain an improved reconstruction. This reversal is referred to as deconvolution, which is a mathematical/computational iterative inversion processing procedure, extensively utilized in astronomy, spectroscopy, and light microscopy to partially restore data distorted by the imaging process [36]. The deconvolution process is constrained. The most common constraint is the imposition of positivity of the deconvolved data [36]. Other stabilizing constraints may include smoothing in real space to suppress high-frequency oscillations. Deconvolution is also very sensitive to noise, and most deconvolution algorithms include regularization parameters whose values are difficult to evaluate theoretically. Additionally, in most cases the deconvolution algorithms will diverge with increasing iterations, building up mottle and noise that obscure the interpretation of the final deconvolved image. Finally, most deconvolution implementations do not have a practical estimate of the error in the converged solution.

Entropy-regularized deconvolution (ER-DC) [37] is formulated to handle data with a weak signal-to-noise ratio, with a regularization term that exploits certain characteristics specific to images originating from crowded molecular environments such as cells. Specifically, in cellular images, high intensities and high second-order derivatives exhibit certain sparse distribution, and this property is exploited by the custom regularization used in ER-DC [37]. This regularization was originally designed for fluorescence images, and this approach was taken

recently for processing of STEM cryo-tomography (CSTET) reconstructions [30].

Since TEM is currently the dominant modality for biological 3-D imaging of cells [38] and its CTF is complex, it deserves a separate study, which is the focus of this paper. The major distinction is that the contrast inversions, which were absent in the STEM data as acquired for tomography, should be accommodated in the construction of the 3D PSF for TEM tomography. Here, a similar approach is taken for TEM. The combined effect of the 2D CTF of the system and the missing wedge are captured in the form a of 3D PSF. We attempt to remove the distortions caused by the 2D CTF and the missing wedge by deconvolving the back-projected 3D image with the aforementioned 3D PSF. We apply this approach to both real data, shown below, as well as to idealized simulated data, discussed in the supplement (Fig **??**) and examine the effects of ER-DC on in real space qualitatively, by Fourier analysis, and by subtomogram averaging.

## 2.2   Materials and Methods

### 2.2.1   Sample Preparation

Yeast *S. cerevisiae* W303a cells were grown at 30°C in YPD media (1% yeast extract, 2% bactopeptone, and 2% glucose) to mid-log phase, after which 5-$\mu$L were deposited in a glow-discharged Quantifoil grid (200-mesh copper R2/1, Electron Microscopy Sciences), followed by manual blotting and plunge freezing in a 50/50 ethane propane mix (Airgas) using a custom-built manual plunger (Max Planck Institute of Biochemistry). Human Embryonic (HEK-293T) cells transfected with LRRK2-I2020T cells were prepared as described in [39]. *In vitro* reconstituted LRRK2-I2020T was prepared as described in [40]. For both yeast and HEK cells, frozen cells were micromachined on a Scios or an Aquilos 2 DualBeam FIB/SEM microscope (TFS). FIB milling was done as described in [6].

### 2.2.2 Cryo-electron tomography

Tilt series were obtained on a 300 kV Tecnai G2 Polara (TFS) or Titan Krios with a field emission gun, a GIF Quantum LS energy filter (Gatan) and a K2 Summit 4k×4k pixel direct electron detector (Gatan). Tilt series were acquired between $\pm$ 50° and $\pm$70° with increments of 2° and 3°, total electron doses between 70 and 100 e$^-$/Å$^2$ at a target defocus of 5$\mu$m, and a pixel size of 2.2 or 3.5Å using the SerialEM software [41] in low-dose mode. Bidirectional or dose-symmetric tomography acquisition schemes were used [42], corrected for the pretilt of the lamella where appropriate. Images acquired on the K2 detector were taken in counting mode, divided into frames of 0.075 to 0.1 s.

### 2.2.3 Tomogram Reconstruction

Tilt series were aligned and dose-weighted by cumulative dose with MotionCorr2 [43]. Dose-weighted tilt series were aligned and reconstructed using Etomo, part of the IMOD package [44]. Patch tracking was used to define the model for fine alignment. The aligned tilt series were reconstructed using WBP to generate the 3D tomograms.

### 2.2.4 Deconvolution

A set of synthetic projections was generated with x and y dimensions and pixel spacing matching the tilt series that was used to make the original reconstructed volume. Each projection had a centered point source that is then convolved with the inverse Fourier transform of the CTF, generated using the defocus and astigmatism parameters estimated by CTFFIND4 [21]. The convolved point source/CTF is then reconstructed using the same WBP used to generate the target reconstructed volume. Finally, the reconstruction is cropped to the same dimensions as the volume to be deconvolved, the 3D FFT of which will be used as the final PSF. Deconvolution is then run for 100 cycles using the generated PSF. A detailed description of the deconvolution procedure can be found in the Supporting Information.

### 2.2.5  Subtomogram Analysis

Microtubule filaments were traced in Dynamo [45] to define coordinates and orientation. Single particles were defined every 4 nm along the filament, and subtomograms with a side length of 66 nm were then extracted from both the back projected and the deconvolved tomograms using these coordinates. For both sets of particles, subtomograms were iteratively aligned over three rounds of two iterations each. The particles were aligned using a spherical alignment mask to minimize bias. For the first round, the alignment was constrained to a 180 degree cone aperture, with no flip allowed and 20 degrees of azimuthal rotation, corresponding to the third Euler angle. Rounds two and three used a 30 and 10 degree cone aperture, respectively, and an azimuthal search range of 10 and 2 degrees respectively. No symmetry was assumed in the alignment. For further details, see [39]. To assess any compensation for the missing wedge, alignment was performed on particles with initial tables describing the particles orientation from 1) a blank table to set all particle orientations to zero, and 2) a random table assigning each particle a random orientation.

To calculate averages for the autophagosome crystal subunit in the WBP and deconvolution tomograms, first 50 particles were identified manually in the deconvolved volume to generate an initial average. This initial average was used as a template for Dynamo's template matching functionality and used to search for similar particles. A cross correlation threshold of 0.38 was selected, below which many particles appeared as false positives by visual inspection. Using the coordinates and putative orientations from template matching, 82 particles were cropped from both the back projected and deconvolved volumes. A global alignment was used on each data set in two (even and odd sets) using the Dynamo subtomogram alignment function [45]. Each half data set was averaged and the directional Fourier shell correlation (dFSC) between the resulting half-averages[46]. The alignment angles from the deconvolved particles were then applied to the WBP particles to create the average shown in Fig. 2.5A and to the relative resolution by dFSC.

### 2.2.6 Simulated data

To validate the effect of deconvolution on the missing wedge under ideal circumstances, a microtubule tomogram was generated from an existing crystal structure (PDB 3J2U). After removing the chains that did not correspond to tubulin subunits forming the microtubule from the model in UCSF Chimera [47], the PDB map was converted to a density map using the EMAN2 functionality $e2pdb2mrc.py$ to convert it to a simulated density map, followed by the $e2spt\_simulation.py$ function to simulate a tilt series [48]. At this stage, the simulated tilt series was an idealized example, with no CTF applied. $e2spt\_simulation.py$ defaults to simulating the particle as if it were embedded in 400 nm of vitreous ice, and the tilt series was binned to make the pixel size 3.3 Å / px to approximate the sampling often used in cellular tomograms. The CTF was simulated and applied to the synthetic tilt series with Priism's $pfocusramp$. The CTF parameters included a defocus of -3.00 um, with no astigmatism. A corresponding point spread function was generated by applying the same CTF to a simulated point source tomogram derived from the simulated microtubule tilt series. The simulated tilt series was reconstructed by weighted back projection, then deconvolved with the corresponding PSF.

### 2.2.7 Data Availability

The tomograms and their corresponding deconvolutions have been deposited in the Electron Microscopy Database. Yeast WBP and deconvolution data can be found at EMD-24433, EMD-24434 respectively. The tilt series and the corresponding tilt and defocus files are deposited at EMPIAR-10762. The inclusion body WBP and deconvolution data can be found at EMD-24435, EMD-24436 respectively. The tilt series and the corresponding tilt and defocus files are deposited at EMPIAR-10761. All the wrapper scripts necessary to perform the steps described here available at https://github.com/Villa-Lab/ER-DC.

## 2.3 Results

### 2.3.1 Electron Tomography Point Spread Function

The key to a meaningful deconvolution is that the synthetic PSF should represent as closely as possible the 3D image of an ideal point source. In the case of TEM, this requires an accounting for the defocus imposed in the image acquisition, which is customarily expressed in terms of a contrast transfer function (CTF). The 3D PSF for deconvolution was computed from simulated projections of a point source with the same dimensions and pixel spacing as the aligned tilt series (Fig. 2.2A). The CTF was first convolved with a projected point-source (Fig. 2.2B), and then a synthetic tilt series was reconstructed to the same dimensions as the original tomogram using the tilt angles represented in the corresponding reconstruction (Fig. 2.2C). This is the real-space PSF, whose 3D FFT serves as the optical transfer function, or kernel, for the deconvolution (Fig 2.2D). The 2D CTFs vary with the gradient of defocus for each micrograph in the tilt series.

### 2.3.2 Tomogram Deconvolution

As a first demonstration of cryo-ET deconvolution we used a HEK cell cultured on-grid that had been FIB-milled to 150 nm thickness. The reconstructed volume contains membranes, microtubules, and a prominent crystalline protein array. The cells were overexpressing human Parkinson's related protein LRRK2-I2020T [39], and the observed repetitive structure is likely an autophagosome, given its double lipid bilayer structure [49]. Contrast is sharp in slices through the XY plane of the tomogram, as expected (blue plane-mid structure, Fig. 2.3B), but contrast and resolution in the Z direction, seen in a slice through the XZ plane (orthogonal green plane in mid structure, Fig. 2.3C) are severely compromised. Furthermore, the reconstructed volume displays a signal both above and below the specimen when observed in the XZ plane. Since the milled slab of material is finite in the z direction, and the sample is imaged in a vacuum, there should be negligible intensity outside the sample volume in the reconstructed data. This is a known artifact of WBP. These image distortions in real space can also be characterized in Fourier
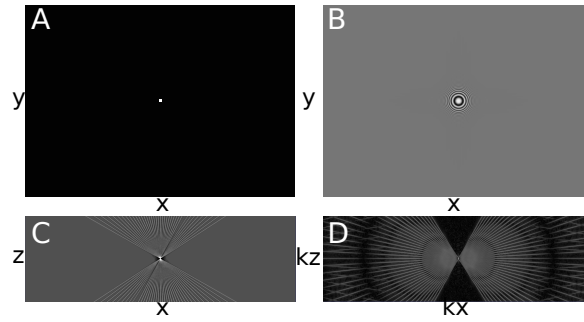
**Figure 2.2.** (A) Synthetic tilt series of a centered point source. (B) Point source tilt series convolved with CTF. (C) Slice of the weighted WBP tomogram of convolved CTF-point source (PSF), xz view. (D) 3D FFT of tomogram showed in C, xz slice.

space, where the real space dimensions $(x, y, z)$ correspond to the Fourier dimensions $(K_x, K_y, K_z)$. The protein array in the real space XY plane appears as a lattice of calculated diffraction spots in the plane $(K_x, K_y)$, as expected (Fig. 2.3E). In the XZ plane, the lattice of spots is sharply truncated at the Fourier planes normal to the limits of the acquired tilts. In summary, WBP suffers from major distortions visible in both real and Fourier space.

The result of 3D deconvolution is shown alongside the reconstruction in Fig. 2.3. Full details appear in the Supporting Information. All processing was performed using the PRIISM image processing software [50]. Briefly, the entropy-regularized deconvolution algorithm from PRIISM was applied using the simulated PSF. While contrast is enhanced in the XY plane, the more striking improvement is seen in the XZ plane (Fig. 2.3J) in comparison with the WBP (Fig. 2.3C). In the deconvolved tomogram, two lipid bilayers are visible (arrow) across the entire sample along Z, as is the crystalline array (Fig. 2.3J). The restoration of information along Z in real space can also be seen in the 3D Fourier transform of the deconvolved volume, which shows increased signal in the previously empty regions corresponding to the missing wedges (Fig. 2.3F,L).

A very effective way to observe the results of deconvolution is to study a small volume of the WBP and/or deconvolved in a dynamic interacting display module, typically a video of the rotating volume. Stereo pairs with additional rotated views are shown for the WBP and deconvolution (supplemental videos RASP1 and RASP2). These may be rocked with a cursor
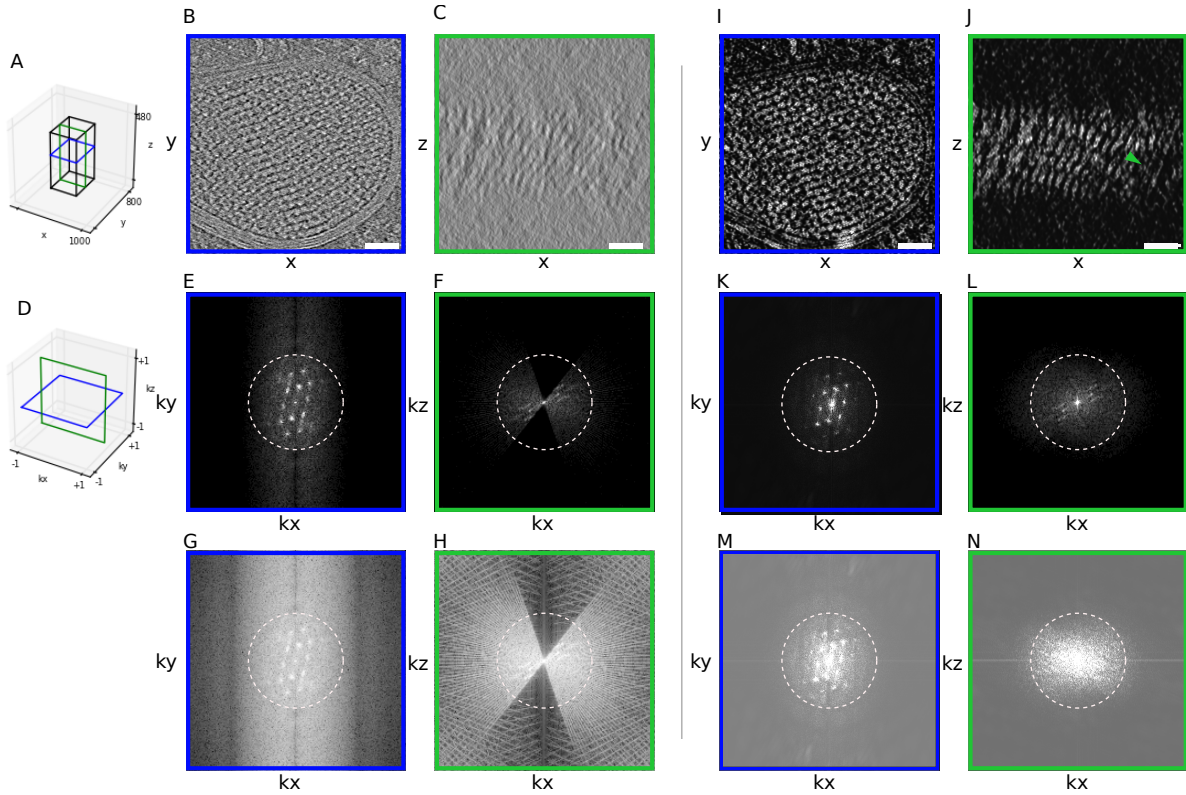
**Figure 2.3.** (A) Schematic of slices used to generate panels B, C, I and J. (B)XY Slice of a tomogram of a HEK cell reconstructed using WBP. Throughout this work, white intensities correspond to high density values. (C) XZ slice of the same tomogram. (D) Schematic to show slices through Fourier space used to generate E,G,K,M in blue and F,H,M,L,M in green. (E,G) Slice through 3D FFT of the WBP corresponding to XY shown with a different distribution of voxel intensities . (F,H) Slice through 3D FFT of the WBP corresponding to XZ shown at two different intensity scales. (I-N) Corresponding results for the tomogram after deconvolution. Scale bars: 100 nm. For reference, dashed circles indicate $0.03 \ \text{Å}^{-1}$ resolution.

bar, as described in Supporting Information, in order to gain an impression in 3D. Distortions along the Z axis associated with the WBP are largely removed after deconvolution. Significant information in the power spectrum appears beyond a spatial frequency of approximately 2.5 nm, which corresponds nominally to the second zero in the CTF for a 6-$\mu$m defocus.

### 2.3.3  A Second Deconvolution Example

For a second example, we applied ER-DC to a tomogram of a relatively thick lamella of *S. cerevisiae* cells (370 nm). Besides the thickness, cryo-electron tomography data of nuclei are
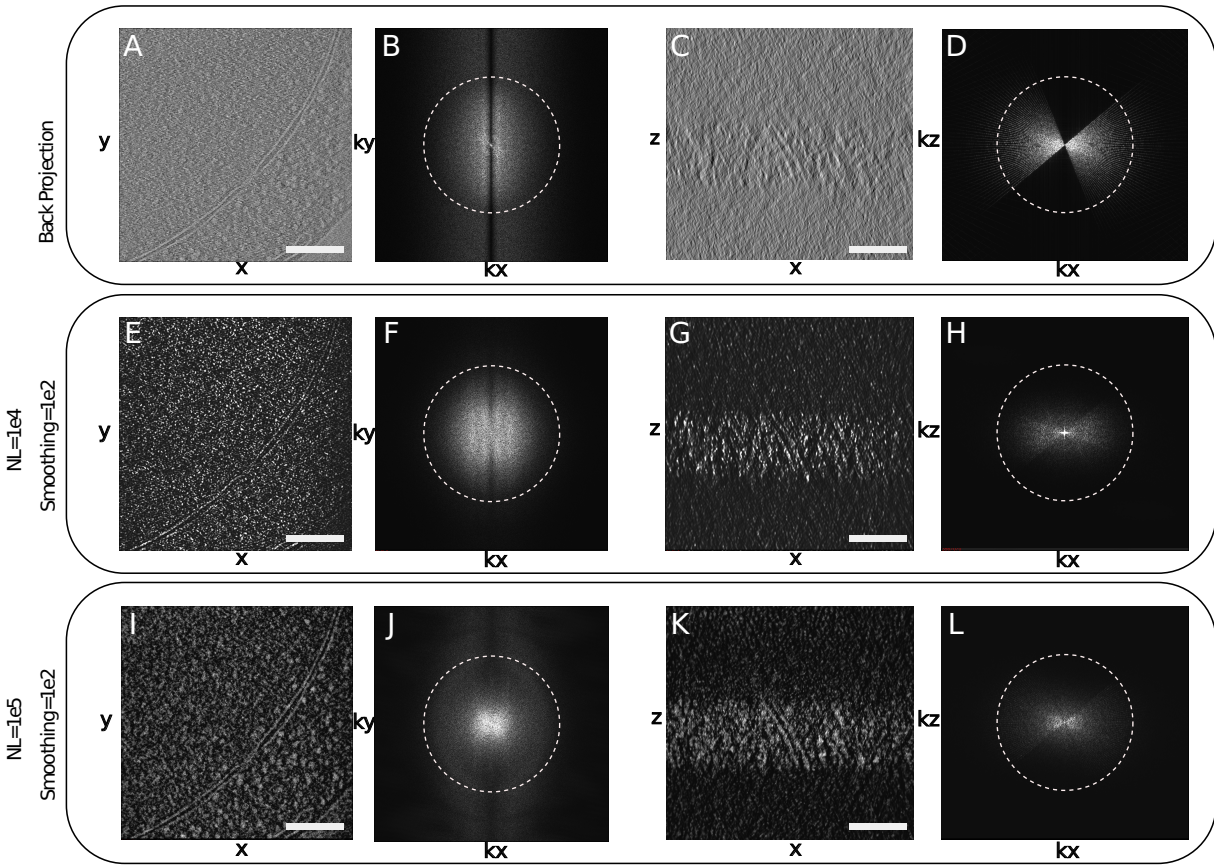
**Figure 2.4.** (A) Central slice (10.6 nm thick) of the XY plane of a WBP tomogram. (B) Fourier transform of A. (C) Central slice of the XZ plane of the WBP tomogram. (D) Fourier transform of C. (E) Central slice of the XY plane of the tomogram deconvolved with a smoothing parameter of 100 and a non-linearity factor of 10,000. (F)Fourier transform of E. (G) Central slice of the XZ plane of the deconvolved tomogram. (H) Fourier transform of G.(I) 10.6 nm slice of the XY plane of a the tomogram from A, deconvolved with a smoothing parameter of 100 and a non-linearity factor of 100,000. (J)Fourier transform of I. (K) 10.6 nm slice of the XZ plane of the deconvolved tomogram from I. (L) Fourier transform of K. Scale bars: 100 nm, dashed circles indicate $0.03 \, \text{Å}^{-1}$ resolution.

challenging samples to interpret as nuclei are densely packed, and lack high-contrast features like membranes, cytoskeletal filaments, or large and defined particles such as ribosomes. As with the deconvolution of mammalian cells, deconvolution provided increased contrast in XY and an improved ability to visually interpret information along Z compared to the WBP. The nuclear envelope is clearly visible in the XY slices of the WBP and the two deconvolutions (Fig. 2.4 A, E, I). In XZ however, no clear structure can be followed in the BP(Fig. 2.4C), but can be

13

more easily followed in the deconvolution (Fig. 2.4 G, K)). Additionally, the missing wedge seen in Fourier space is filled in by the deconvolution process (Fig. 2.4 H, L)). By utilizing rotating angle stereo-pair renderings of the volume (RAPSs), one can compare the WBP and deconvolved volumes in 3D (supplemental videos RASP3 and RASP4). In the BP, there is little distinguishable structure as the volume rotates. In contrast, fine features can be identified at every angle, such as the nuclear envelope, as well as densities that could correspond to chromatin and nucleosomes. The 3D-FFT of the deconvolution (Fig. 2.4), KxKz view, shows the missing wedges being filled in, indicating that the deconvolution process helps correct for these artifacts, even in challenging samples.

### 2.3.4   Deconvolution and Subtomogram Analysis

Subtomogram analysis is an approach to protein structure determination *in situ* [11, 51, 52, 53, 54, 55, 56, 57, 58, 59, 60, 61, 62, 63, 64, 65]. Similarly to single particle analysis, of which it is an extension to 3D, averaging multiple examples of images that represent particles of the same kind serves to reduce noise. If the molecules lie in random orientations, 3D averaging can also be used to compensate for the missing wedge [11]. The crystalline-like body seen in Fig. 2.3 provided an interesting test case for averaging where orientations were determined to be uniform by translational symmetry in the crystal (Fig. 2.5). Therefore, only select orientations are represented in the sample. First, we attempted to align the crystal subunits over $360^0$ in $\theta$ and $\phi$ on the WBP reconstruction. This resulted in an alignment that was dominated by the missing wedge, a common pitfall in subtomogram averaging, and produced a structure that was strongly elongated(Fig. 2.5A). Second, we used the same particles, but this time from the deconvolved data set. Alignment and averaging resulted in a structure that resembled much better the unit of the crystalline array in the original tomogram (Fig. 2.5E). Third, we averaged the WBP particles using the transformations determined by the deconvolution alignment. In this last case, we obtained a structure similar to the one obtained from deconvolution-aligned and deconvolution-averaged particles (Fig. 2.6B), demonstrating that the alignment of subtomograms

is improved by deconvolution. This tomogram was acquired from a HEK cell overexpressing human LRRK2 [39]. While the identity of the molecules forming the crystalline-like array was not specifically established (*e.g.*, by CLEM) and the number of particles in this tomogram is severely limited (82), the overall shape of the deconvolved average resembles the cryo-EM structures of LRRK2 determined both *in situ* bound to microtubules [39] and *in vitro* [40].
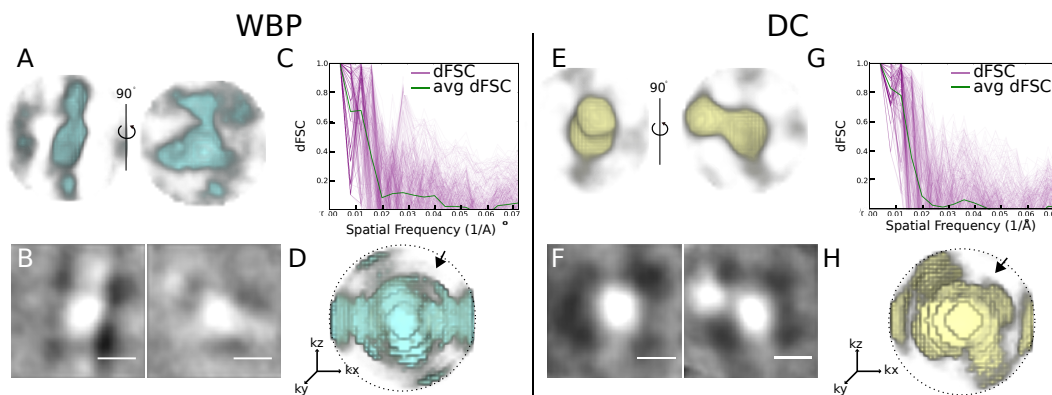


**Figure 2.5.** (A) Two views of the crystal body average of WBP subtomograms. (B) Central 1.4 nm slice of WBP crystal body subtomogram average. (C) 3D-FSC curves generated from two half-map averages of the WBP crystal body subtomogram average. Green line is the average, pink lines are individual directional FSCs. D) 3D render of dFSC curves; arrowhead denotes the center of the missing wedge. (E-H) corresponding averages and FSCs derived from the deconvolved volume. Scale bars: 10 nm. dFSCs shown out to Nyquist resolution ($0.07Å^{-1}$).

Fourier shell correlation (FSC) is widely used in single particle cryo-EM [66], as a metric of the resolution of a molecular structure. It is a quantitative measure of similarity, typically implemented in cryo-EM by comparing two structures, each generated from a half data set. The comparison is done by correlating shells of the 3-D Fourier transform of each of the half maps. Standard FSC compares global similarities, correlating all orientations contained within a shell, giving a single curve for the entire structure as a function of spatial frequency. Resolution is then quoted as the inverse spatial frequency where the correlation drops below an accepted threshold. Directional FSC (dFSC) is a variant in which all Euler angles are explored for frequency comparison, and provides a representation of resolution in all directions [46]. dFSC was applied to two half-map averages from the crystalline array in the WBP, and then in the deconvolved averages to assess changes in resolution in any direction between the WBP

15
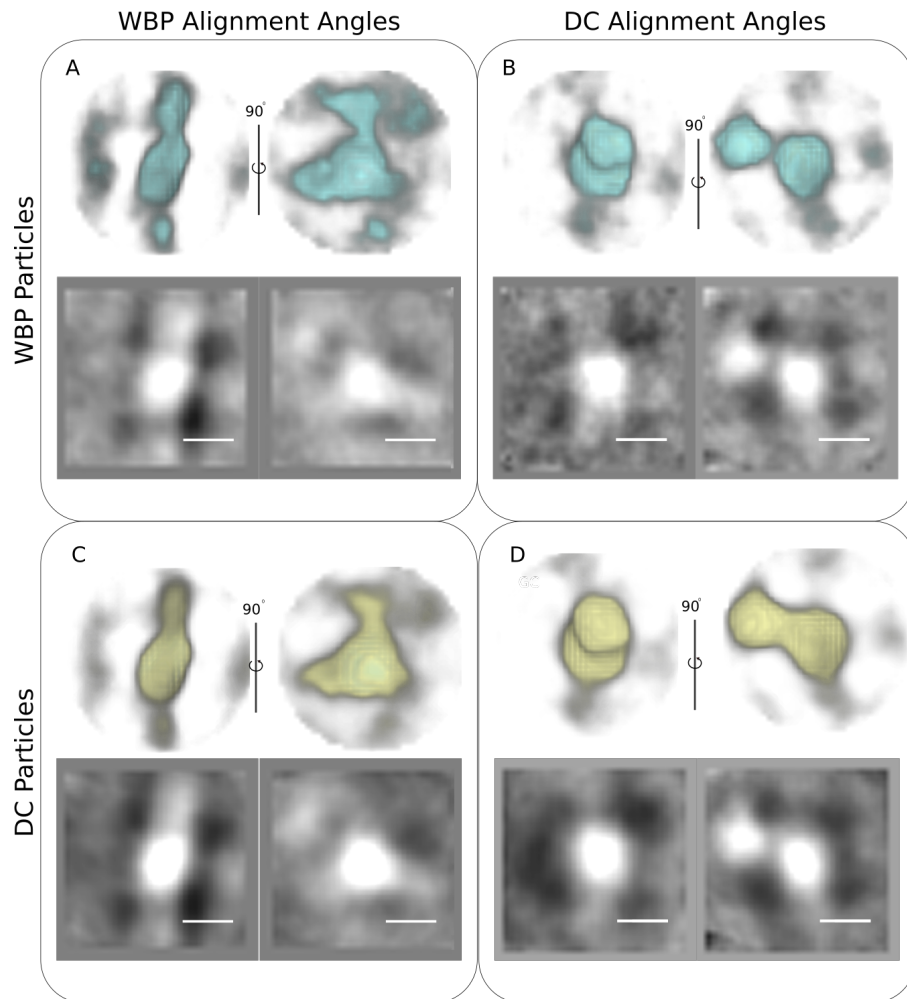
**Figure 2.6.** Comparison of WBP aligned particles and DC aligned particles. (A) Volume views of the crystal body average generated by aligning WBP subtomograms. (B) Volume views of the crystal body average generated by aligning WBP subtomograms using alignment parameters generated by aligning DC particles. (C) Volume views of the crystal body average generated by aligning DC subtomograms. (D) Volume views of the crystal body average generated by aligning DC subtomograms using alignment parameters generated by aligning WBP particles. Scale bar: 10 nm

(Fig. 2.5 C) and deconvolution (Fig. 2.5G). The resolution from the averaged dFSC curves is similar for the deconvolved and the WBP reconstructions ($\sim 53\text{Å}$), using the gold-standard FSC; however, the curves of the averaged and individual dFSC have higher correlation at this and higher resolutions. This is evident when comparing the 3-D rendering of the dFSC for the WBP (Fig. 2.5 D) and deconvolution (Fig. 2.5H), where the resolution is anisotropic (lower correlation in the area of the missing wedge denoted by an arrow) for the WBP but not for the deconvolution. Further, higher resolution is found in the deconvolution reconstruction.

To investigate the effects of deconvolution in the alignment of the particles and the improvement of the average due to the missing wedge separately, we chose to use microtubules, since their structure is well established, as are the pipelines for subtomogram analysis. We analyzed a tomogram of reconstituted microtubules decorated by the Parkinson's related protein LRRK2$^{RCKW}$[40]. In the tomogram, it is evident that the deconvolution process increased the contrast between the microtubules and the surrounding media, and we again see a reduction in XZ distortions (Fig. 2.7A,B,D,E), as well as a corresponding filling of information in the missing wedge in Fourier space (Fig. 2.7C, F). Microtubule subtomograms were extracted from both the WBP and deconvolved volumes using the filament tracing function in Dynamo[45]. The subtomograms were independently aligned and averaged as described in [39] and in Materials and Methods (Fig. 2.10 A, B). Note that the contrast between protofilaments is distinctly sharper for the deconvolved data. However, this method of alignment includes an azimuthal randomization that is specifically designed to average out the missing wedge in the final average. To assess the effect of deconvolution specifically on the missing wedge, we ran the alignment without this randomization step, that is with the missing wedge always in the same orientation, as it exists in the original particles. Compared to the WBP, the deconvolution-processed average shows increased distinction between protofilaments in the direction of the missing wedge (Fig. 2.10D). Lastly, we used the alignment parameters generated from the azimuthally zeroed deconvolved subtomograms to the WBP particles to generate a WBP average (Fig. 2.10E). Here, the deconvolution-aligned WBP average still shows a prominent missing wedge, similar to the

17

WBP average generated by aligning WBP particles. This indicates that the improvement in the average from the deconvolved particles is not simply due to improved alignment, but that the filling of the missing wedge is reducing distortions in XZ, thereby improving the resulting subtomogram averages.
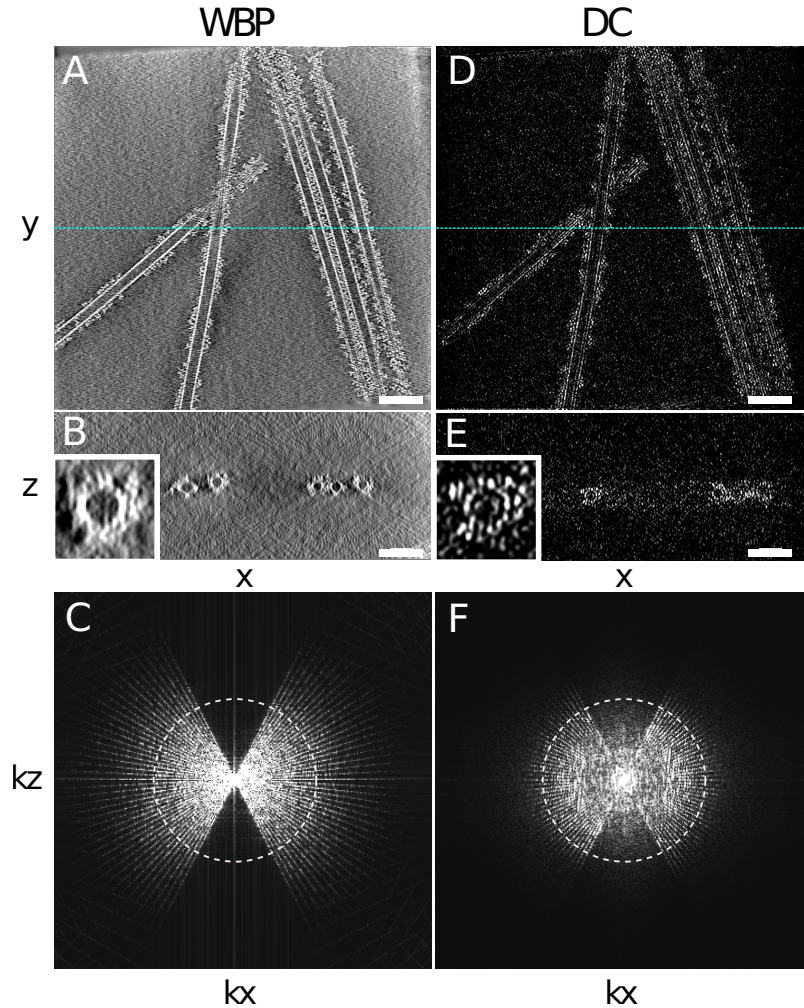


**Figure 2.7.** (A) XY slice of the WBP-reconstructed tomogram containing microtubules. (B) XZ view of the tomogram in A; blue dashed line in A corresponds to the slice shown. (C) kxkz view showing the missing wedge. (D) XY of the deconvolution tomogram. (E) XZ of deconvolved tomogram in D; blue dashed line in D corresponds to the slice shown. (F) kxkz of the deconvolved tomogram. Scale bar = 50 nm, dashed circles indicate $0.06\,\text{Å}^{-1}$ resolution

In addition to the experimental data explored in this paper, we used simulated tomography data was to investigate the effect of DC on a system with a known solution. While the noise models in simulated data are not fully comparable to experimental data, we reasoned that
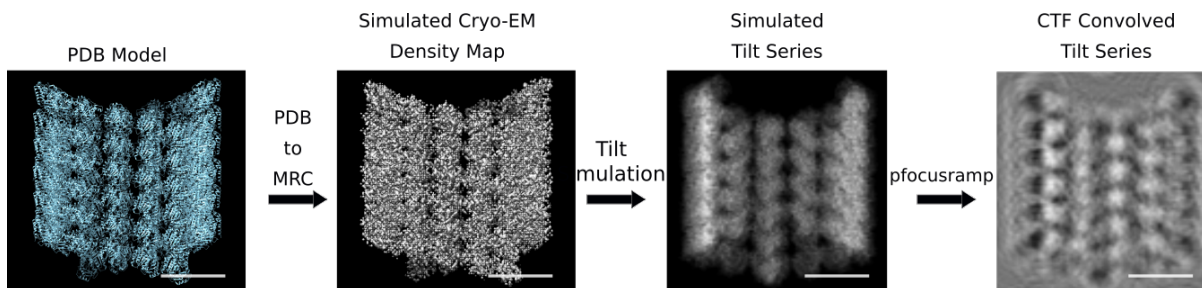
**Figure 2.8.** Workflow for simulation of tilt-series. A simulated cryo-EM density (MRC format) is created from an atomic model of a microtubule (PDB format). Then, a tilt series of is simulated from the map and then convolved with a -3.00 $\mu$m defocus CTF. Scale bar: 10 nm.

we should apply DC to these data with the expectation that it recovers the initial structure accurately by filling in the missing information in the missing wedge area. We picked a X-ray crystallography structure of a microtubule from the Protein Databank (PDB-3J2U) to generate a simulated cryo-EM map at 3.3Å resolution using EMAN2 [48]. Then, we simulated a tilt series of the density map (Fig 2.9), which was reconstructed using our standard WBP (Fig 2.8 B). Deconvolution was applied to this simulated tomogram, resulting in a near complete refilling of the missing wedge (Fig 2.8 D,G), demonstrating that DC works in idealized cases.

## 2.4 Discussion

We have successfully applied ER-DC to cryo-electron tomograms, and demonstrated enhanced contrast compared to the WBP reconstructions, as well as reduced resolution anisotropy along the Z axis. In real space, one can follow membranes in the XZ plane of the deconvolved volume that were hardly visible in the WBP. In Fourier space, it is clear that portions of the missing wedge are filled in, and the distribution of voxel intensities changes significantly as a result of deconvolution. However, there are still several considerations for TEM deconvolution, and these are further discussed in the Supporting Information.

First, the reality is that deconvolution acts as a filter for the data. The intensity of each voxel is modified in some fashion, and care must be taken in interpreting the deconvolved volume. Deconvolution has two parameters, for non-linearity and smoothness, and the optimal values
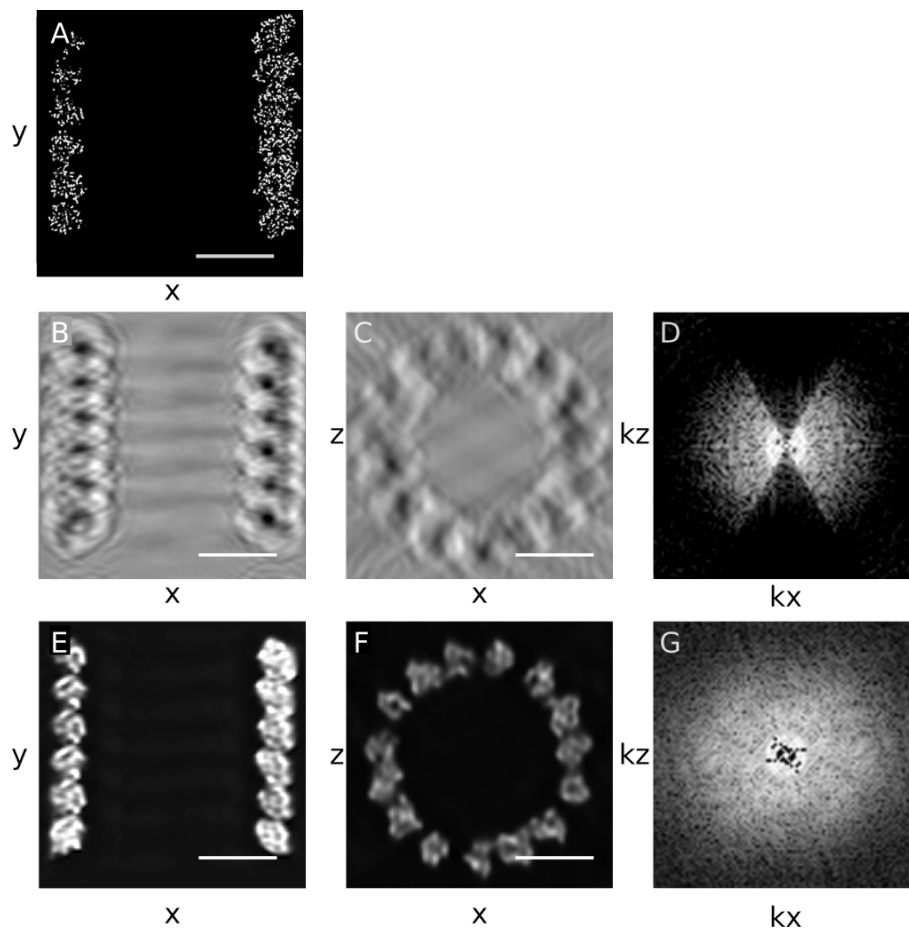
**Figure 2.9.** Back projection of simulated tilt series and corresponding deconvolution. (A) Central slice of a simulated the microtubule cryo-EM map. (B) XY central slice of the tomogram reconstructed using WBP from the CTF-convolved simulated tilt series. (C) XZ central slice of the tomogram in B. (D) kXkZ fourier spectrum of (C). (E) XY central slice of the deconvolution. (F) XZ central slice of the deconvolution. (G) kXkZ fourier spectrum of (F). Central slice thicknesses are all 10 Å. Scale bar: 10 nm

must be determined experimentally by systematically varying the parameters over several orders of magnitude; the parameter search quickly settles into basic convergent deconvolved images that look biologically reasonable (e.g. membrane bilayers are visible, ribosomes are distinct, etc.). At the end of the deconvolution process, one can usually settle on a few deconvolved images coming from a close smoothness parameter. These different deconvolved images are studied side-by-side comparing 3-dimensional volumes for details. The side-by-side images are very similar to one another, but subtle features between them exist. Crucial are the orthogonal Z image planes for judging smoothness parameters and structure. There are a number of considerations for the deconvolution process, discussed in the Supporting Information.

How does one know if the deconvolved structure is credible? In addition to the side-by-side study of several smoothness deconvolved images, a control raw WBP image must be studied alongside the deconvolved images, at several intensity scalings of the WBP data. Any feature uncovered in the deconvolved data would be searched for in the raw WBP data control, and would have to be present in the WBP control. However, in our experience, the deconvolution process has never been observed to invent a structure that is not present in the WBP raw data control [30].

This study makes the statement that the missing wedge of information is substantially filled by deconvolution. Visually and in Fourier space representation this is the case; however, this statement needs caution. We do not know if deconvolution will improve Z resolution for certain kinds of data, intensities, or different structures *e.g*., of various sizes. It is possible that spaced periodic structures positioned on top of one another along Z in a tomogram are not resolved correctly in the deconvolved data.

A second point in the deconvolution discussion centers on what mathematics allows unobserved data to propagate from areas of observed data, into their correct structural space. Since all image information can be decomposed into 3-dimensional Fourier representation, one is, in essence, saying that there is information in one region of Fourier space that can be extrapolated correctly into other regions of Fourier space by the deconvolution process. There are
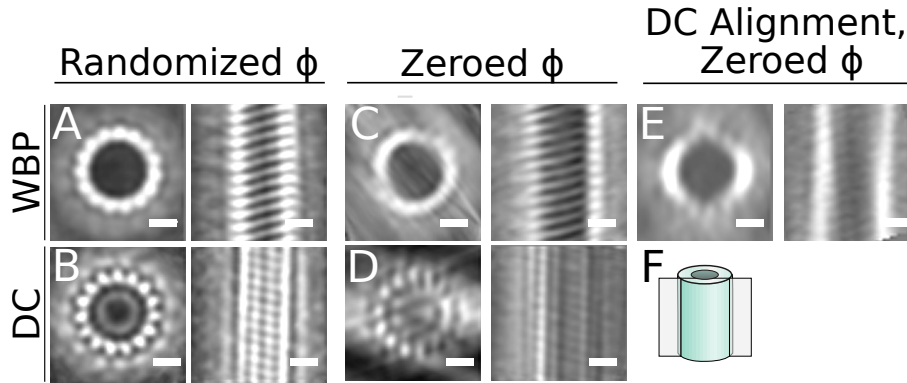
**Figure 2.10.** In all panels, top and side views of the average are shown for the microtubule average obtained under the specified conditions (A) Average from the WBP tomogram, using a randomized azimuth-angle ($\phi$) averaging approach to compensate for the missing wedge [39]. (B) Average from the deconvolved tomogram using the same randomized $\phi$ scheme. (C) Average from the WBP tomogram, with initial constant $\phi$ angles for all particles, allowing the missing wedge to affect the average. (D) Average from the deconvolved tomogram using the same constant $\phi$ scheme. (E) Average generated by applying the alignment parameters from the deconvolution uniform starting azimuth/restricted rotation alignment to the the WBP particles. (F) Schematic showing the location of the slice on the right-hand side image in each panel. Scale bars: 10 nm.

two examples from the inverse problems literature to reassure that such extrapolated information can indeed be real. The first one is called "Analytical Continuation" ([67], and references therein), which is known in optics literature. The Analytical Continuation (AC) conjecture, taken from [67], states: All image information can be decomposed into a Fourier transform, and a spatially bounded region of Fourier space can be expressed as an analytical function. The analytical function can be exactly known for a small region, and if there is no noise, the entire analytical function can be determined/extrapolated by AC. The extension can continue indefinitely, and this is a hallmark of AC [67]. Noise is critical and the analytical values become small as iterations progress as the function get extended to higher resolution regions of Fourier space, reasons AC is little used (but see [67]). In the case of ER-DC, noise is heavily suppressed and resolution extensions required are modest, suggesting that AC might work.

The second one is called compressive sensing reconstruction, used in modalities such as magnetic resonance imaging [68] and tomography [69]. It involves high-quality reconstruction

from highly under-sampled Fourier data and tomographic projections with a limited set of angles with regularization constructed using derivatives. Because of the way the derivative operator is related to the measurement operator (tomographic projection or Fourier transformation), high quality reconstruction becomes possible from sparse Fourier samples or from tomographic projections from a limited set of angles. Although these theories are not directly extensible to our recovery problem, they reassure that extensions in Fourier space are possible, and hence the filled-in missing wedges may be trusted if the resultant structures in the real space appear plausible.

Another independent argument supporting why the missing wedges could correctly be filled can be given from a statistical viewpoint. Recall that the regularization used in the ER-DC enforces certain hypothesized joint distribution of intensity and second-order derivative magnitude. It turns out that the back projected images deviate significantly from this joint distribution. Hence, the minimization involved in ER-DC brings in a proper filling on the wedges such that: 1) the resulting real space image is consistent with the measured projections, and 2) the resulting real space image better matches with hypothesized distribution.

Thirdly, deconvolution could have an impact on the electron dose required to obtain a suitable tomogram. The deconvolution process might allow other dose reduction steps, such as fewer tilts and lower beam intensity. In addition, there are several aspects of the deconvolution process that can be improved, and are described in the Supporting Information.

The deconvolution process filling in the missing wedges in Fourier space allows biological structures to be followed in 3-dimensions. This resolution is adequate to see, for example, gaps between the 10 nm nucleosomes allowing a chromosome path to be followed. One imagines a two step process for cellular tomography: first, the path of a structure is followed with the architecture discerned, a process greatly improved by deconvolution. Subsequently, once an architecture is determined, molecular features can be superimposed using averaging methods and molecular modelling [39].
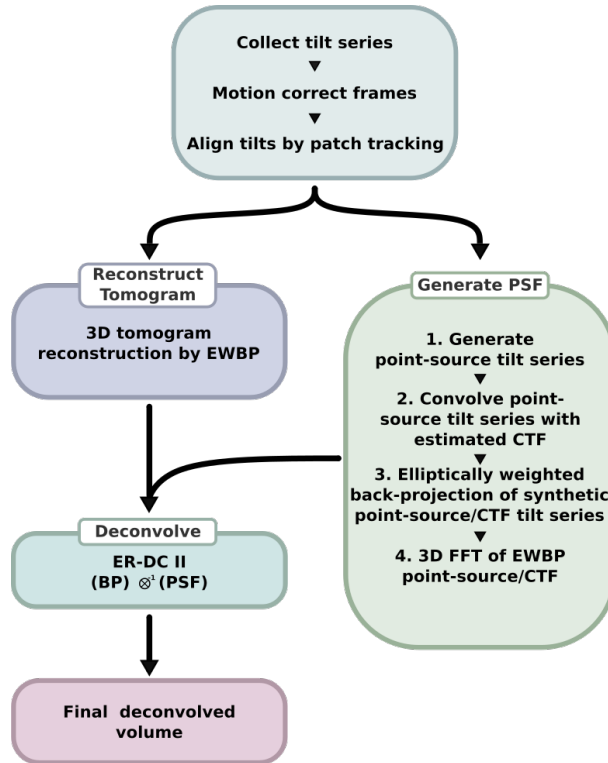
**Figure 2.11.** Schematic of the deconvolution workflow.

# 2.5 Supporting Information

## 2.5.1 Detailed Deconvolution Workflow

**Computing the Transfer Function for the Deconvolution**

To include the microscope contrast transfer function (CTF) in the transfer function for deconvolution, the per-projection defocus and astigmatism parameters were determined by running CTFFind 4.0.7 [21] for each of the projections in the aligned and motion-corrected tilt series. The parameters used for CTFFind were the tomogram pixel spacing (2.9 or 3.6 Å, depending on magnification), 300 kV for the acceleration voltage, 2.27 mm and 2.7 mm for the spherical aberration of the Polara and the Titan Krios respectively, 0.07 for the amplitude contrast, 512 for the size of the power spectrum, 44 and 11 Å for the minimum and maximum resolutions respectively, 10000 and 100000 Å for the minimum and maximum defocus respectively, 2500 Å for the defocus search step, and 100 for the expected astigmatism. For those projections whose

radially averaged spectra from CTFFind did not have clear rings from the zeros in the contrast transfer function, the means of the defocus and astigmatism parameters from the other projections were used.

The transfer function for deconvolution were computed with these steps (SI Appendix Fig. 1):

1. Generate synthetic projection data for a centered point object interacting with the electron beam. That synthetic projection data incorporated the per-projection defocus estimates from CTFFind.

2. Reconstruct that synthetic projection data with the same reconstruction method as used for the experimental tilt series.

3. Compute the three-dimensional discrete Fourier transform of the result of step two to get the unnormalized transfer function.

4. Divide the values in the unnormalized transfer function by its value at the zero frequency so that applying the transfer function to a sampled volume does not change the volume's mean intensity value.

The result of step two is the sampled point spread function (PSF) for the combined process of imaging the point object at different tilt angles and reconstructing it.

Synthetic projection data were generated in two stages. First, a series of images are generated to match the number of projections and the dimensions of the measured tilt series and the dimensions of the tilt series after binning by two and trimming for the reconstruction region of interest. All samples in those images are zero except for the central pixel which has a value of one. Those images are then blurred by the modeled microscope CTF incorporating the per-projection defocus estimates. The initial point source tilt series is made using PRIISM 4.6.1, and a text file, `tilts.txt`, that has the tilt angles, one per line and in units of degrees, for the measured tilt series. This was achieved by first taking the 2D FFT of each projection of

the aligned tilt series, then thresholding the result to give a single pixel central point with an intensity value of 1.

```
insert_tilts tiltseries.ali tilts.txt
FTransform2D tiltseries.ali tiltseriesfft.mrc -center_zero
    -real_complex_full -same_units -x=0:(Xdim-1) -y=0:(Ydim-1)
Threshold tiltseriesfft.mrc synproj_noblur.mrc -result=mask
    -not_below=6 -mode=short
```

Using the file named `synproj_noblur.mrc` from the first stage, `pfocusramp` from PRIISM 4.6.1, and a text file named `defocus.txt` with the estimated defocus values, one per line in units of microns and written with a negative sign to match PRIISM's convention for defocus, the second stage can be implemented by running `pfocusramp` as follows:

```
pfocusramp synproj_noblur.mrc synproj_blur.mrc -amp=0.07 -axis=0 -cs=2.27
    -deftxt=defocus.txt -kv=300 -mtf=1:5.2279:0:50 -op=apply -nxstripe=1
```

That includes a Gaussian envelope, $e^{-5.2279q^2}$ where q is the spatial frequency in cycles per sample, to approximate the observed loss of power in the radially averaged spectra from CTFFind.

The weighted back projection of the blurred synthetic projection series was computed to get the PSF using PRIISM 4.6.1's `ewbp` as follows:

```
ewbp synproj_blur.mrc psf.mrc -reconxz=1000:480 -sizexz=1000:480 -iy=0:799
    -filter=2 -hdfilt=1 -moderec=2
```

The command for the measured tilt series specified the sizes in terms of the unbinned coordinates; here they are in the binned coordinates and are one half the size.

PRIISM 4.6.1's FTransform3D was used to compute the three dimensional discrete Fourier transform of the PSF to get the transfer function:

```
FTransform3D psf.mrc tf.mrc -same_units -shift=499:240:399
```

In computing the Fourier transform, the origin of the spatial domain was shifted to match the peak of the PSF so that applying the transfer function to a volume does not shift the contents of the volume. Also, to match what is expected by the deconvolution software, the metadata for the sample spacing was kept in the spatial domain units rather than converting it to the equivalent spacing in the frequency domain.

**Computing the Weighted Backprojection to be Deconvolved**

The tomogram to be deconvolved was reconstructed by elliptically weighted back projection from the aligned and motion-corrected tilt series. The tilt series were all single-axis from -70 to +50 degrees with approximately two degrees between each projection. The tilt series was reconstructed using the ewbp function included in PRIISM 4.6.1. The reconstructions were binned by a factor of 2 relative to the original tilt series to decrease computation time.

The commands within PRIISM used to compute the reconstruction were:

```
AppendRes tfile 2 1


appl_prm tfile ifile -iprmfile=afile -dimxy=xdim:ydim -iv=0:ntilt:1

    -iref=-1 -imform=2 -pcbase=0.05 -tilt_offset=0 -statfile=none -res=1

    -fullsize=3838:3710 -rscale=2


ewbp ifile rfile -reconxz=1960:960 -sizexz=2000:960 -iy=0:1599

    -filter=2 -hdfilt=1 -moderec=2 -rscale=2
```

where `tfile` is the name of the tilt series file in MRC format and tilt angles in the extended header. `afile` is an alignment file that in these studies specified no further changes to the data. That file is text with two empty lines followed by one line per projection in the tilt series. The $j^t h$ of those lines has ten values separated by one or more spaces. The first is the

value of *j*. The next eight values are zero, one, zero, zero, one, one, one, and zero, respectively. Those specify no change to the rotation, no change to the magnification, no changes to the translation, and no transformation of the intensities. The final value on the line is the tilt angle, in degrees. `ifile` is the name to use for an intermediate file, in MRC format, that has the tilt series reinterpolated to account for the change in the region of interest for the reconstruction. `rfile` is the name of the file, in MRC format, which will store the weighted backprojection.

**Deconvolving the Weighted Backprojections**

The deconvolution used Muthuvel Arigovindan's ER-Decon II algorithm as implemented in PRIISM 4.6.1. Before the deconvolution, the contrast of the weighted backprojection was reversed, such that densities appeared as bright signal. That was done by multiplying the values by minus one. Since the deconvolution has a background determination step, the value of the constant added when reversing the contrast will only shift the value of the background determined during the deconvolution and not affect the deconvolved volume. The deconvolution was implemented as follows where `ewbp_rev.mrc` is the name of the file with the contrast-reversed weighted backprojection and `tf.mrc` is the name of the file with the normalized transfer function:

```
core2_decon ewbp_rev.mrc deconvolved.mrc tf.mrc -alpha=1e5
    -lamf=5e2 -lampc=0 -lampos=1 -ncycl=100 -linesearch=2014
    -regtype=ma -nonorm_otf -nzpad=zdim -oplotfile=cost_history.txt
    -rfactor
```

The options, `-alpha` and `-lamf`, set the key tunable parameters for the algorithm, $1/\varepsilon$ and $\lambda$, respectively, as they are denoted in [37]. The option, `-ncycl`, sets the number of deconvolution iterations to perform. The `-lampc`, `-lampos`, `-linesearch`, `-regtype`, and `-nonormotf` options were kept constant. The first of those disables the cone filter that the ER-Decon II implementation uses to precondition the problem. The calculations for the cone

28

filter assume that the deconvolution is for optical microscopy and don't match conditions when deconvolving a weighted backprojection. The `-lampos` option specifies the relative weighting for the positivity term in the cost function for the deconvolution. The value used here includes the positivity term with no additional weighting factor in addition to that set by `-lamf` which weights all the regularization terms in the cost function. The `-regtype` option selects the same form for the cost function as in [37]. The `-linesearch` option selects a revised line search algorithm. To use the line search algorithm in [37], one would use `-linesearch=2013` rather than `-linesearch=2014`. The `-nzpad` option sets the padded size in z to use during the deconvolution. The value used matches the input size in z so no padding is included. The `-oplotfile` option causes an extra output file to be generated that records the value of the cost function for the deconvolution at each iteration. The `-rfactor` option adds additional data to that file to record the r-factor measure for the blurred deconvolved guess and the input volume to be deconvolved.

**Incorporating a Spatial Constraint in the Deconvolution**

While not applied in this study, a spatial constraint may also be incorporated in the deconvolution, implemented by adding a term to the cost function that is the sum over positions of the squared product of the current guess, g(r), with a spatial mask, M(r),

$$\lambda \lambda_w \Sigma_r (g(r)M(r))^2$$

Where the mask is not zero, nonzero intensities in the guess are penalized. The first scaling factor multiplying the sum is the overall scaling factor, $\lambda$, for the regularization terms added to the cost function. The second scaling factor, $\lambda_w$, controls the relative weight of the spatial constraint to the other regularization terms. Setting that scale factor to zero nullifies the spatial constraint so the cost function is identical to the one in [37]. The addition of the term to the cost function changes equation S22 in [37] paper by adding a term,

$$\lambda \lambda_w g(r) M(r)$$

, to the left hand side. It also changes the diagonal approximation in equation S29 by adding a term,

$$\lambda \lambda_w g(r) M(r)$$

, to the right hand side. For the computation of the initial guess, contribution from the spatial constraint is ignored.

An implementation of the ER-Decon II algorithm with the spatial constraint term is available in PRIISM 4.7.0.

For the experiments performed, the mask for the spatial constraint was not changed during the deconvolution iterations, and a value of one was used for $\lambda_w$. The command options to include the spatial constraint in PRIISM's core2_decon are:

$$-lammask = 1 - imask = mask\_file$$

where mask_file is the name of the file, in MRC format, that contains the values for the spatial constraint mask. The mask must match the dimensions of the padded input volume.

**Constructing a Spatial Constraint Mask**

A hard binary mask was constructed for the spatial constraint as follows:

1. In every 5th slice perpendicular to the tilt axis of the deconvolved weighted backprojection, image coordinates are selected corresponding to the top and bottom edges of the slab of material appeared to intersect the left and right edges of the deconvolved weighted backprojection.

2. A linear least squares fit is found for each of the four sets of coordinates for the corners of the slab, upper left, upper right, lower right, and lower left to define the boundaries of the volume.

3. For each slice perpendicular to the tilt axis the vertices of the parallelogram whose left and right sides match the left and right edges of the deconvolved backprojection are calculated using the linear models from step two for the coordinates of each corner.

4. For the spatial constraint mask in a slice perpendicular to the tilt axis, any sample outside the parallelogram computed in step three, is set to one, and any sample inside the parallelogram is set to zero.

**Perturbing Deconvolution Iterations**

Some experiments stopped the deconvolution after a certain number of cycles, modified the guess, and then used the modified guess as the starting point for more deconvolution iterations. The implementation of ER-Decon II in 4.7.1 allows the initial guess for the deconvolution to be provided as a file in MRC format. The command line option that sets the initial guess is

```
-guess=file_name
```

where `file_name` is the path to the file, in MRC format, with the values for the initial guess.

**Computing Fourier Transform Results**

Fourier transform results for the undeconvolved or deconvolved weighted backprojection were computed as follows:

1. A 400 x 400 x 400 box was extracted whose bottom lower left corner was at the sample coordinates, (300, 40, 200), where the first coordinate is the direction perpendicular to the tilt axis and axial direction, the second coordinate is in the axial direction, and the third coordinate is along tilt axis.

2. The mean of the extracted volume was subtracted from that volume's values.

3. The result of step two was apodized by applying a triangular window to each dimension. The triangular window is zero at the first sample in the dimension, linearly increases to one at the 200th sample, and then linearly decreasing to .005 at the last sample.

4. Three-dimensional discrete Fourier transform of the result of step three was computed and, for display purposes, the zero frequency term was shifted to be at sample coordinates (199, 199, 199) in the 400 x 400 x 400 volume.

**Computing the Cylindrically Averaged Fourier Transform Amplitudes**

The procedure to compute the cylindrical average, an $nr \times nz$ element array called `cyla`, of the Fourier transform amplitudes in a $n \times n \times nz$ array was as follows:

1. Set $nr$ to be $floor((n-1)/2)$, where $floor(v)$ is the largest integer less than or equal to $v$.

2. For each plane, $iz$, in the transform perpendicular to the axial frequency axis:

    (a) Initialized a $nr$ element counter array, $icount$, to zero and a $nr$ element amplitude sum array, $asum$, to zero.

    (b) For each element, coordinates (ix, iy), in the plane:

        i. Computed the amplitude, $a$, of the Fourier transform.

        ii. Compute the radial frequency, $k$, from the coordinates. Since the zero frequency component in $x$ and $y$ had coordinates of $(nr-1, nr-1)$ and the pixel spacing and dimensions in $x$ and $y$ are isotropic, $k$ is $\sqrt{(ix-nr+1)^2+(iy-nr+1)^2}$.

        iii. If $k$ is less than $nr$ , let $ik$ be $floor(k)$. Add one to $icount[ik]$ and add to $asum[ik]$

3. Set $cyla[iz, j] = asum[j]/max(icount[j], 1)$ for $j$ between 0 and $nr-1$, inclusive.

For display in the figure, only every other frequency, from the zero frequency, was displayed.

Using commands from PRIISM, the computation of the Fourier transform of a 400 x 400 x 400 volume from v.mrc, which has the full weighted backprojection or deconvolution of the weighted backprojection, and computation of the cylindrical average, ad.mrc, of the amplitudes was:

```
FTransform3D v.mrc f.mrc -x=300:699 -y=40:439 -z=200:599 -subtract=mean
    -triangular=0.5:0.5:0.5  -real_complex_full
    -center_zero -same_units
Flip f.mrc ff.mrc -xz
RadProj ff.mrc af.mrc -format=mrc -polar -average -components=amplitude
    -center=199:199:199 -r=0:200 -nr=200 -theta=-180.01:180.01 -ntheta=1
Flip af.mrc a.mrc -xz
Decimate a.mrc ad.mrc -x=0:199 -y=1:399 -factor=2:2
```

Flip was used after the Fourier transfer because the output of the weighted backprojection has the axial dimension as the second fastest varying axis in the file. For the averaging step, it needs to be the third fastest varying axis. The second use of Flip wass to convert a nr x 1 x nz file to a nr x nz x 1 file.
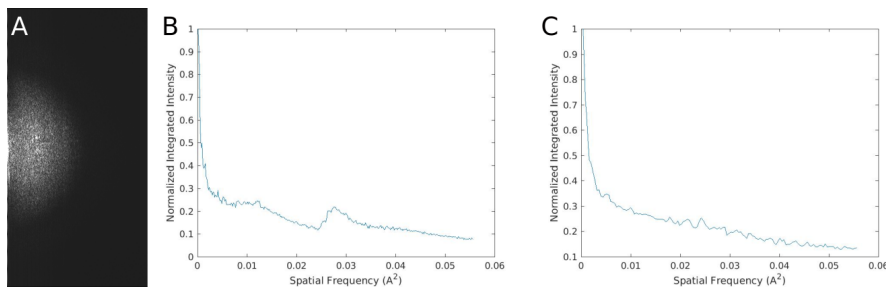


**Figure 2.12.** Cylindrical averages of 3D FFT of DC tomogram. (A) FFT of tomogram to be radially averaged. (B) Relation of average amplitude to frequency in kr. C) Relation of average amplitude to frequency in kz.

## 2.5.2   Notes on the DC Methods

If the centering convention for the tilt series alignment is not consistent with the conventions used by `appl_prm` and `ewbp`, that would introduce some error in the reconstruction. `ewbp` in version 4.7.1 of PRIISM has ways to override its default centering conventions so one could correct for a mismatch without regenerating the aligned projections.

The placement of the projection of the point object in the synthetic projections used to compute the PSF does not exactly match up with `ewbp`'s centering conventions. By default, `ewbp` places the x coordinate of the center of the aligned projections at 0.5 * (nx_projection – 1) and assumes the projection rays through the centers intersect at (0.5 * (nx_recon – 1), 0.5 * (nz_recon – 1)) in the xy planes of the reconstruction. Since the projection and reconstruction dimensions used here are even, those conventions put the x coordinate of the center of the projection at 499.5 and the center of the reconstruction in the xz plane at (499.5, 239.5). For the synthetic projections, the center of is defined at 499.

A separate deconvolution was performed using `ewbp` 4.7.1 to override the default centering convention. The deconvolution result from that transfer function was, qualitatively, much the same as the transfer function generated with the procedure in the methods. For future work, `ewbs`'s conventions in the computation of the transfer function should be overridden to avoid the mismatch. That would mean replacing:

```
ewbp synproj_blur.mrc psf.mrc -reconxz=1000:480 -sizexz=1000:480 -iy=0:799
    -filter=2 -hdfilt=1 -moderec=2
```

with:

```
ewbp synproj_blur.mrc psf.mrc -reconxz=1000:480 -sizexz=1000:480 -iy=0:799
    -filter=2 -hdfilt=1 -moderec=2 -pcen=499 -reconcen=499:399
```

The shift specified for the Fourier transform of the PSF would also change. Replace:

```
FTransform3D psf.mrc tf.mrc -same_units -shift=499:240:399
```

34

with:

```
FTransform3D psf.mrc tf.mrc -same_units -shift=499:239:399
```

The computation of the PSF assumes that there's something in the system that will guarantee that the point object ends up being band-limited to the frequency range set by the pixel spacing. If one isn't willing to assume that, one could generate synthetic projections that have 1/m times the pixel spacing and have m times the samples in each dimension, apply the microscope CTF as desired, reconstruct the synthetic projections, and then finally bin the result by m in each dimension. For a sufficiently large m, likely 3 or 4 in this case, that would account for the high frequency information that would be aliased into the measurement.

Once the PSF has been generated, a range of DC parameters are tested and compared to choose which combination of smoothing and non-linearity parameters is optimal (SI Appendix Fig 2.13, S 2.14, our choice for optimal combination highlighted in blue). The optimal parameter combination is judged based on the filling of the missing wedge as seen in Fourier space, as well as the change in contrast in the real space image. We typically find the optimal smoothing parameter to be between 400-600, and the non-linearity parameters give optimal results around 10000.

### 2.5.3   New DC Directions

There is no question that the DC process changes intensity distributions, sharpening features and minimizing fog/noise. The process does not alter the monotonic relationship of the intensities (i.e. does not invert contrast), only the relative difference in intensity. Flips of intensities from positive to negative or the reverse have never yet been observed in the DC process. Still, intensity changes must be interpreted with caution. Do all areas of the intensity histogram contain similar amounts of information post DC? For example as a function of scaling the DC image and comparing the bright areas of the histogram to weak intensity areas, are there differences in Fourier space DC representation ( see especially [30])? There are additional
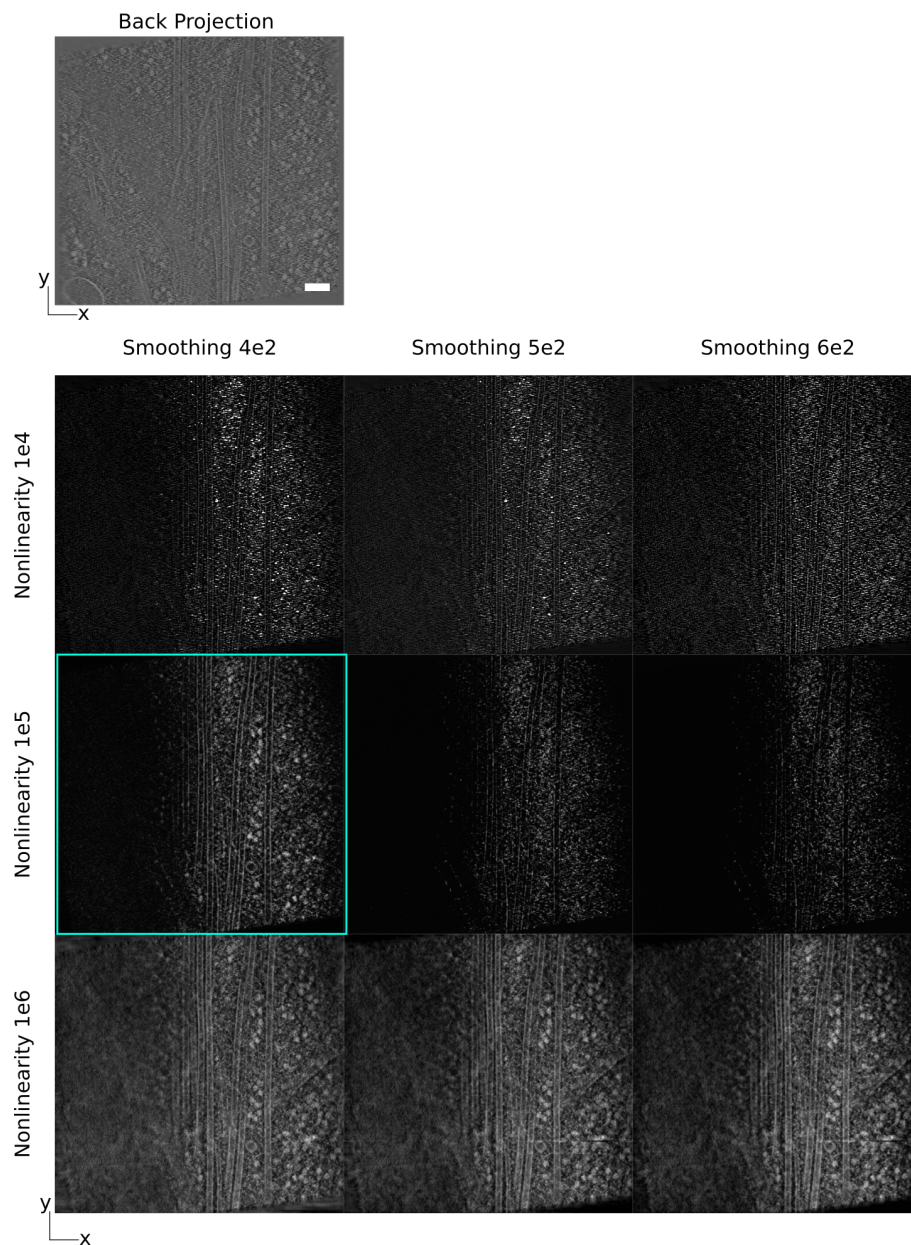
**Figure 2.13.** Matrix of deconvolution results at different smoothing and non-linearity parameters (XY projections). Scale bar: 100 nm.
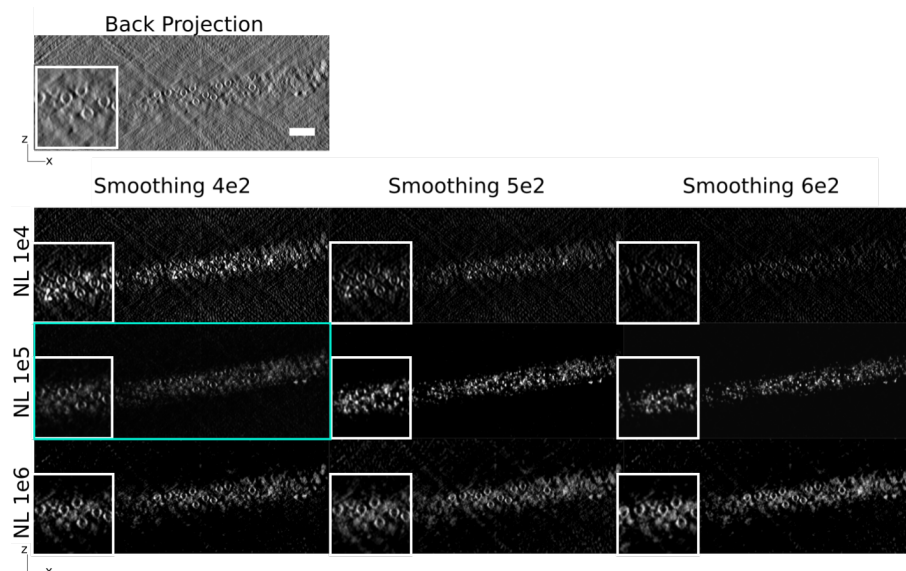
**Figure 2.14.** Matrix of deconvolution results at different smoothing and non-linearity parameters (XZ projections).Scale bar: 100 nm.

aspects of the DC process, such as extension of the iteration number( up to 1000 iterations), and other DC steps that will be addressed in future work.

It is important to carefully scrutinize DC images for differences, artifacts, or errors, as this procedure is still new. One does not know if the parameters for the cytoplasm are different from those optimal for the nucleus, for example. One does know that once parameters are known for a region of the tomogram, it is possible to move the DC area/volume around the large tomogram and get equivalent DC. Still, the optimal parameters have been similar for all tomograms deconvolved.

Could the DC process reduce the electron dose required for the cryo-ET? With the improvements gained from DC, it is conceivable that the number of tilt steps required might be reduced. Alternately, a lower electron dose could potentially be used, followed by image restoration by DC. DC could also enable the study of slightly thicker volumes (200-400 nm) by reducing the noise inherent in these thicker images. It is known that for this thickness range, about half of electron scattering events are inelastic. These inelastically scattered electrons are separated from the elastic (zero loss) scatter events by an energy filter at great effort/ expense.

37

The inelastic events do not contribute to usable image information, creating instead a fog of background noise. Might the DC improve tomograms obtained without an energy filter?

The DC process might also benefit from a large reduction of defocus, while still recovering the contrast. The PSF of this lower defocus tilt series would be much simpler. If this were possible, DC could act as a computational substitute for the expensive/complex phase plates.

For computing how the defocus varies across an image with a nonzero tilt angle, $pfocusramp$ assumes that the defocus parameter you supply correspond to the defocus near the center of the image (zero-based pixel coordinates, $(floor(nx/2) - 1, floor(ny/2) - 1)$, to be precise). At the pixel, $(ix, iy)$, in zero-based indices, $pfocusramp$ will add to the defocus amount.

```
p * sin(t) * dot_product(
  (ix - floor(nx/2) - 1, iy - floor(ny/2) - 1),
  (cos(a), sin(a))
)
```

where a is the tilt axis orientation angle, t is the tilt angle, and $p$ is the pixel spacing. In other words, if the tilt axis is vertical ($a = 0$), the tilt angle is positive, and the center of the image is underfocused, the points to the right of center will be less underfocused; points to the left of center will be more underfocused.

Lastly, while the DC process is computationally reasonable time frame, a rewrite into modern GPU technology would greatly speed up the computational time.

### 2.5.4  Movies, and Their Discussion

Because the advantage of DC relates to improvements in 3-D resolution, it is important to visualize and interpret the data in 3-D. One effective way to visualize DC data is to use stereo pairs (SP) where two angular views are displayed side by side, and viewed such that the brain interprets the two images as one 3-dimensional scene. To do this, a 3-D region (cube) of interest

is selected from the original 3-dimensional DC image. Two projections of that cube are then generated, with a 6-12 degree difference in the projection angle. Then, by viewing the SP straight on (12-24 inches away) with slightly crossed eyes, one can visualize a third image of the volume in 3D.

Viewing a volume in motion can also aid in interpretation of structures in the DC volume. By animating the rocking of an SP (rotating angle stereo pair, or RASP) while visualizing the cube in 3-dimensions, the SP are rotated in the computer and the SP, offset in 6-12 degrees, are generated and viewed. In addition, the cube of data can be tilted at several large angles to generate multiple angular views, each in different orientations, rocked and in stereo (SP). We recommend to generate and visualize movies in stereo, and take advantage of the play bar to allow control of the rocking. Information in the SP does require careful study(and considerable time to perceive the structures). The DC process is not perfect, and the differences in resolution (in Z, for example) help many times to reconcile and bring into perspective the different structures in the 3-dimensional volume.

## 2.6   Acknowledgements

**Figure 2.15.** Microtubule subtomogram averages and their dFSCs.(A) Average from the WBP tomogram, using a randomized azimuth-angle ($\phi$) averaging approach to compensate for the missing wedge [39]. (B)dFSC corresponding to (A). (C) Central slice of the dFSC from (B). (D) Average from the WBP tomogram, with initial constant $\phi$ angles for all particles, allowing the missing wedge to drive the alignment. (E) dFSC corresponding to (D). (F) Central slice of the dFSC from (D). (G) Average from the DC tomogram, using a randomized azimuth-angle ($\phi$) averaging approach to compensate for the missing wedge. (H) dFSC corresponding to (I). (I) Central slice of the dFSC from (H). (J) Average from the DC tomogram with initial constant $\phi$ angles for all particles, allowing the missing wedge to drive the alignment.(K) dFSC corresponding to (J). (L) Central slice of the dFSC from (K). Cyan lines in plots represent dFSCs of angles sampled during tomography. Red lines in dFSC plots represent those angles that comprise the missing wedge, thick red line is their average. Black line represents the global average of all dFSCs. Scale bars: 10 nm. Dashed circle indicates Nyquist resolution, $0.059 Å^{-1}$.

40

## 2.7 Supplementary Files

**RASP1**

Rotating angle stereo-pair movie of back projected tomogram of crystalline body.

**RASP2**

Rotating angle stereo-pair movie of deconvolved tomogram of crystalline body.

**RASP3**

Rotating angle stereo-pair movie of back projected tomogram of yeast nuclear periphery.

**RASP4**

Rotating angle stereo-pair movie of deconvolved tomogram of yeast nuclear periphery.

# Chapter 3

# Characterizing Silicon Nitride as an Alternative Experimental Platform for Cryo-Electron Tomography

## 3.1   Introduction

Despite the exceptionally detailed views of the cellular interior attainable with cryo-FIB-ET, its full potential for cell biology is still limited by a number of technical challenges on the experimental side [22, 70, 71]. One such challenge is that the substrate most often used in cryo-FIB-ET is a metal mesh overlaid with a layer of porous amorphous carbon (Fig 3.3 A) [72, 73]. These grids have several disadvantages from a cell biology perspective. First, they present an atypical surface for cell growth. This impedes direct comparisons between cryo-FIB-ET data and data from cells growing on solid surfaces such as glass or plastic, given the effects the mechanical properties of the environment can have on cellular processes [74, 75, 76]. Second, the surface of carbon grids is uneven both in height and in surface properties, with parts of the film unsupported and others resting on top of metal crossbars [77, 78]. Finally, the amorphous carbon film is physically fragile and susceptible to chemical degradation, limiting the types of experiments that can be performed using carbon film grids as a substrate.

When looking for platforms to overcome these limitations, several factors must be considered. First, the new grids must be compatible with the holders currently used in cryo-FIB-

ET, referred to as "autogrids" [6]. This means they must be slightly under 3 mm in diameter and no more than 150 $\mu$m thick so that they can be clipped in place. Next, the material should not have its own crystalline structure, as this would result in regular scattering that would show up in the resulting tomogram [79]. Finally, the material must be thin enough that the thermal mass will not impede proper vitrification during plunge freezing. Vitrification is a form of freezing where water is cooled at such a rate that that the hydrogen bonds that stabilize into crystalline ice don't have time to form, resulting in a glass-like (vitreous) form of ice that preserves samples in their native state. For water to vitrify, it must be cooled at a rate on the order of $1e6\ K\ s^{-1}$ [80]. Mammalian cells are already near the size limit for what can be vitrified with simple plunge freezing, with even two cells in close proximity resulting in crystalline ice, so any new substrate cannot be one that slows down the effective rate of cooling.

One potential alternative with all of these characteristics are silicon nitride (SiN) grids [81]. Comprised of a thin silicon nitride membrane atop a silicon support frame (Fig 3.3 B), the SiN surface is flat, hard and uniform, and like glass coverslips they can withstand chemical treatments for controlling cell adhesion [82, 83, 84, 85], making them a promising alternative on paper. While these properties would make SiN an improvement over carbon grids for cryo-FIB-ET based cell biology experiments, every step in the existing cryo-FIB-ET workflow must first be adapted to this new platform (Figure 3.1). The process for getting a grid all the way through the cryo-FIB-ET pipeline is as follows:

- Glow discharging the grid in order to increase adsorption of whatever surface treatment is being applied. A grid can be incubated in a solution extracellular matrix such as fibronectin directly after glow discharge, which will enable cells to adhere to all parts of the grid. Alternatively, if one wishes to control where cells adhere, micropatterning is an option.

- (Optional) After glow discharge the surface can be passivated by incubating the grid in poly-lysine-g-PEG. This layer can then be selectively removed by photoscission, confining cells to those areas that have lost the PLL-g-PEG layer.

- Growing cells on grids, or deposit them immediately prior to plunge freezing.

- Drying the grids without dessicating the sample and plunge into liquid ethane-propane for vitrification.

- Clipping the grids into holders referred to as "autogrids." An autogrid is an annular piece of of copper that can hold an EM grid in place by use of a small copper c-clip. The grid is clipped into the autogrid under $LN_2$ and is now ready to be loaded onto a TEM equipped with a cryo-stage.

- (Optional) If a specific molecule is being targeted, fluorescence data are necessary to locate it on the FIB. For this, samples are mapped on a cryo-fluorescent microscope. This map can then be used as a reference to target cells with your features of interest.

- FIB milling of the cells in the sample into thin lamellae (Figure 3.2).

- Collecting tilt series on the lamella in the TEM.

With such an extensive workflow and so many potential failure points, cryo-FIB-ET is a demanding technique. Here we demonstrate the use of SiN grids for growing and freezing cells, as well as its limitations with respect to cells requiring FIB milling.

## 3.2 Methods

### 3.2.1 Grid Dryer Construction and Control

The most common approach for drying grids is by blotting away liquid with filter paper. The grids are blotted exclusively from the back (non-cell side), as the filter paper will damage cells if in direct contact [6]. This approach would not work on SiN grids, due to the lack of pores through which liquid may travel. The drying device is constructed around a manual plunging rod [86] provided by Tim Baker. The rod was enclosed in a humidity chamber constructed from 3/16" acrylic. It functions by passing a curtain of humidified air over both sides of a SiN grid.
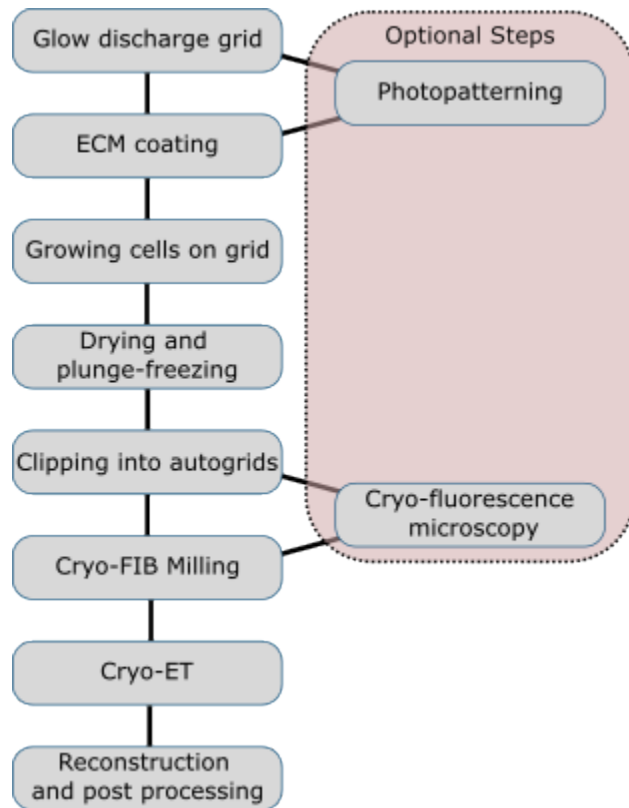
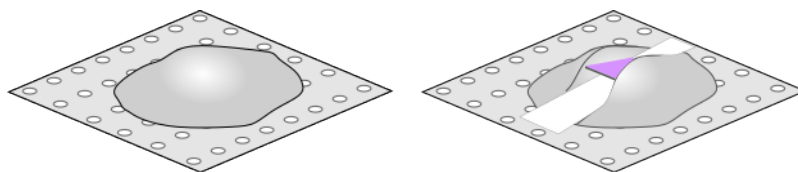**Figure 3.1.** Overview of steps in the cryo-FIB-ET workflow, with optional steps highlighted in red.



**Figure 3.2.** Schematic of cell grown on porous carbon film prior to FIB milling (left) and after FIB milling with a lamella highlighted in purple, being supported on either side by the rest of the cell material (right).

Housed within the humidity chamber is a bifurcated nozzle that forms two opposing sheets of air that blow liquid off either side of a grid as they pass over it (Fig 3.4). The height of the nozzle is controlled by a stepper motor driving a cart moving along a piece of aluminum 80/20 railing using a 3D printed rack and pinion system (Fig 3.4B, 2-3). It is controlled through a RapsberryPi (Pi) model B single board computer running the Raspian operating system. The Pi sends signals to a microstep driver (SMAKN TB6600) via the Pi's inbuilt GPIO pins, controlling the speed of descent of the nozzle. Power is supplied to the motor and driver via a 12V DC 3 amp power supply. The stepper motor itself (VEXTA PK245-02AA) is attached to a pinion printed in PLA plastic (thingverse.com, thing:944471, dreyfusduke). The pinion matches a corresponding rack attached to the nozzle, which descends past the grid as the pinion turns. The air pushes away excess liquid from the grid surface while leaving a thin layer in place and maintaining the cells in a hydrated state. The length of the rack is such that once the grid passes through the airstream and excess liquid is removed, the plunge rod is released and the grid is plunged into a mixture of liquid ethane and propane at liquid nitrogen temperature (-190°C). The level of drying is determined by 1) the nozzle's speed of descent, controlled using the RaspberryPi, and 2) the air pressure, controlled by a regulator determining the air pressure going into the humidifier, and a second controlling the pressure out of the humidifier.

## 3.2.2    Nozzle Construction

The nozzle is made of three layers of clear acrylic sheet joined together with 3M adhesive. The top and bottom layers are solid 3/16" acrylic, while the middle layer is 0.25mm acrylic with the with a narrow (0.5mm) bifurcated channel for directing sheets of air to either side of an EM grid. Both sides of the middle sheet were covered with 3M adhesive, and the desired shapes were cut with a laser cutter (Fig 3.4 C). A hole was drilled in the top piece for a 1/8" hose barb fitting. The pieces were then aligned and pressed together to make the device. The final channel has cross sectional dimensions of 10 mm x 0.5mm.
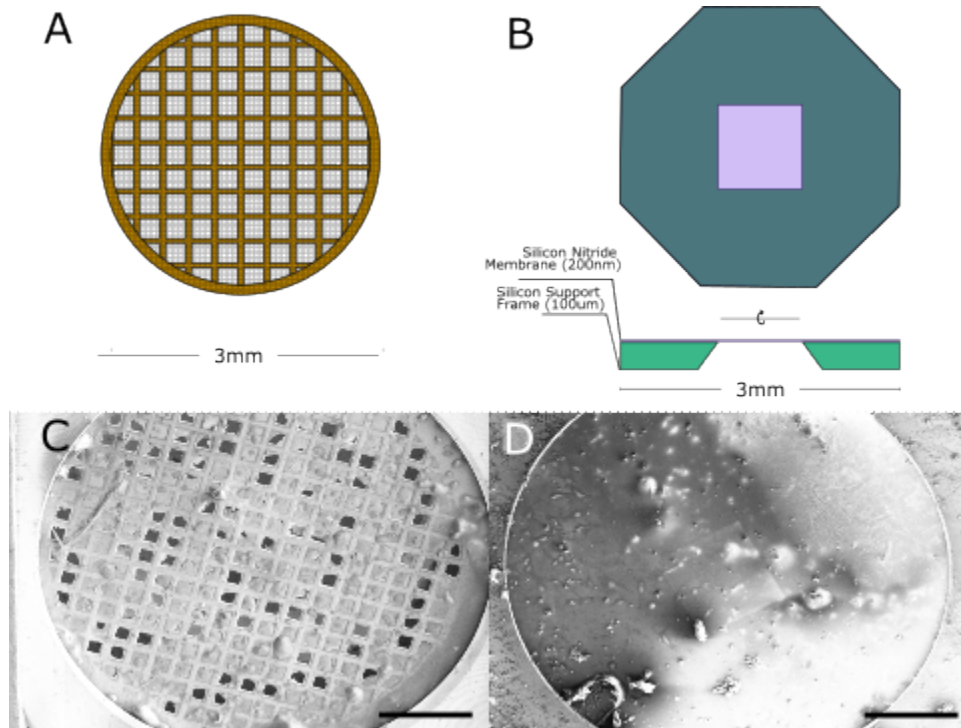
**Figure 3.3.** Comparing Metal and Silicon Nitride Grids. (A) Diagram of metal and carbon foil grid. (B) Diagram of silicon nitride EM grid. SiN grids consist of a thin membrane of silicon nitride atop a silicon support frame with a window etched into the silicon. (C) Frozen metal grid with cells. Cracks and ruptures can be seen in the carbon foil. (D) Frozen silicon nitride grid with cells. No damage is visible on the grid's surface. C, D scale bars $500 = \mu$m.
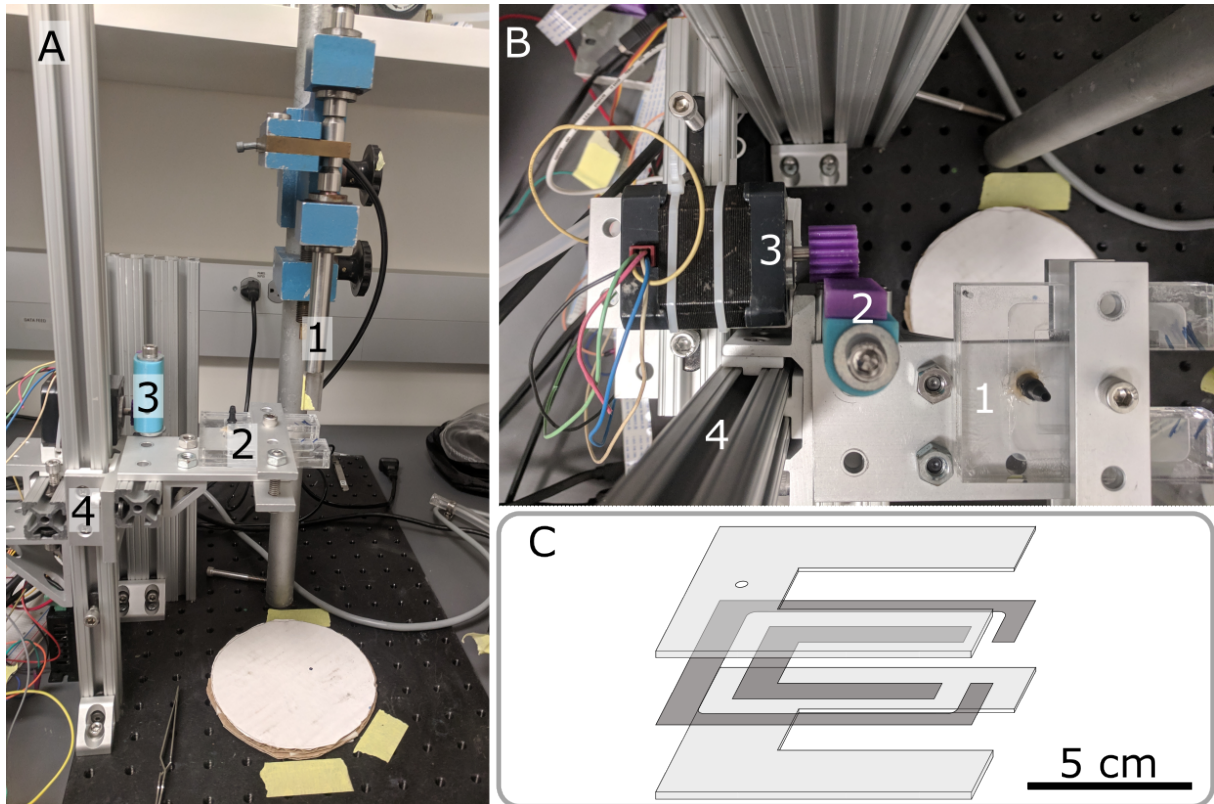
**Figure 3.4.** SiN Grid Air Drying Device. (A) Overview image of the drying device. A pair of tweezers holding a SiN grid is attached to the plunge rod (1). An acrylic nozzle (2) is lowered by a rack and pinion system (3) driven by a stepper motor along a piece of 80/20 guide rail (4). (B) Top view of nozzle and height control setup with the nozzle (1) controlled by the rack and pinion (2) driven by a stepper motor (3)along a guide (4). (C) Nozzle construction, with a channel cut out of a 0.25mm acrylic sandwiched between to layers of 3/16" acrylic bonded together using 3M double sided tape.

### 3.2.3 Carbon Coating

Prior to growing cells on grids, they are first carbon coated to improve cell adhesion and reduce surface charging while FIB milling [87]. Carbon filament is cut and fixed to the electrodes of an Edwards Auto 306 Carbon Coater. Silicon nitride grids are placed on a glass microscope slide inside the carbon coater's bell jar, and the chamber is pumped down to $< 5e - 6$ Torr. Once at vacuum, the carbon filament is outgassed by sending current through the filament until it is white hot. After outgassing the carbon filament, the protective shield is moved out of the way to allow carbon to coat the grids, at which point a current is again run through it until white hot, and held for 5 seconds. The chamber is then vented and the carbon coated grids removed.

### 3.2.4 Cell Culture

Grids were glow discharged in a PELCO easiGlow glow discharge system (Ted Pella) for 60 s at 0.2 mbar at 20 mA, followed by incubation in 50 ug/mL fibronectin solution in Dolbecco's modified Eagle's medium (DMEM). Grids were placed in a humidity chamber, consisting of a petri dish with damp filter paper (Whatman Grade 1), at 37°C for 30 minutes, followed by 30 minutes at room temperature under UV light in a cell culture hood. NIH-3T3 cells were harvested at 80% confluency and diluted to 1.5e4 cells/mL in 20 mL of DMEM supplemented with 10% fetal calf serum and 1% penn-strep antibiotic. Diluted cells were then added to grids, which were affixed to the petri dish with a layer of transparent silicone. The cells were allowed to grow on the grids for up to 16 hour prior to plunge freezing [6].

### 3.2.5 Micropatterning

SiN grids are first glow discharged in a PELCO easiGlow glow discharge system (Ted Pella) for 60 s at 0.2 mbar at 20 mA to activate the surface and improve adsorption of the non-fouling layer [76]. Each grid is then placed onto circular PDMS pedestal in a glass bottom cell culture dish (Alvéole). They are then incubated in a solution of 0.1% Poly-L-Lysine for 1 hour at room temperature. The grids are then washed 3x in milliQ water, then 3x in HEPES

49

pH 8.5. Grids are then incubated in a 100 mg/mL solution of PEG-SVA in HEPES 8.5 for 1 hour. After incubation in PEG-SVA, grids are washed 2x with HEPES 8.5, then 3x in MQ water. PEGylated grids were then patterned with UV light projected using the PRIMO digital micromirror device (DMD) micropatterning system mounted on a Nikon T$_i$2. A photoinitiator solution is added to the coated grid, which is exposed to patterned UV light ($\lambda$ = 375nm) for a total energy of 900 $\mu$Joules/mm$^2$ from the PRIMO, resulting in patterned photodegradation of the PLL-g-PEG [76]. The grid is then incubated in a solution of 1 mg/mL fibronectin that adsorbs onto the patterned areas, defining where cells may adhere.

## 3.2.6 Plunge Freezing

A hot plate holding the water bottle for the humidifier is turned on. Humidified air is used to prevent evaporative drying from the air stream, which will change the osmotic environment and causing unwanted cell stress responses. An metal cup is then cooled with liquid nitrogen and filled with a 50:50 mixture of ethane and propane. The ethane cup is placed under the plunging rig and a grid is carefully removed from the culture dish with self-closing tweezers. Media trapped in the tweezers is quickly wicked away using filter paper and the tweezers are attached to the plunge rod with lab tape. Dry air is run through a regulator, into a humidifier, and through a second regulator before being directed through the nozzle. The air supply is turned on to a pressure of 10 PSI at the second regulator, and the stepper motor is started. The nozzle descends past the grid and the humidified air pushes off excess liquid while leaving behind hydrated cells. Once the nozzle has dropped past the grid, the rod is released using the foot pedal and the air supply is shut off. Once the grid has been plunge frozen, it is transferred under liquid nitrogen to storage boxes and stored in liquid nitrogen for later processing.

## 3.2.7 Cryo-FIB Milling

As stated above, most cells are require thinning to achieve high resolution cryo-ET. After grids have been frozen they are clipped into autogrids under liquid nitrogen. Clipped grids are

then loaded under LN$_2$ onto a specialized shuttle, which is then transferred under vacuum to a cryo stage in an FEI Scios (for later samples, a TFS Aquilos) dual beam SEM and focused ion beam (FIB) microscope. Once cells are located on the grid window, the grids are coated in a layer of organometallic platinum via a gas injection system to reduce the charging effects of milling and produce smoother and more consistent results. An overview image of the grid is taken using the SEM which is used to identify cells to be milled. Once targets are identified, eucentric height is found for each position. Eucentric height is the stage height where the SEM and FIB converge on the same spot of the sample, allowing for the milling progress to be observed by SEM. The stage is then tilted to the desired milling angle (typically 5$^o$-10$^o$ relative to the FIB) [88]. The lower the milling angle, the longer the resulting lamella will be. Default milling patterns are used consisting of two rectangles that have a width of 10 $\mu$m and variable height depending on the sample. At the start of milling, these two patterns are positioned 2 $\mu$m apart vertically. Rough milling with a beam current of 300 pA is used to remove the bulk of the cellular material. Lamellae would then be thinned using an intermediate beam current of 100 pA, followed by a last thinning and polishing step at 30 pA, resulting in lamellae 100-300 nm thick [88, 6].

## 3.3 Results

### 3.3.1 Silicon Nitride Sample Preparation

When seeding cells on untreated SiN grids, the cells mostly failed to adhere to the surface (Fig 3.5 A). Cell attachment was similar on grids that had been glow discharged SiN grid and incubated in a solution of fibronectin (Fig 3.5 B). Adhesion could be further improved by adding a thin layer of amorphous carbon to the grid prior to glow discharge/fibronectin coating (Fig 3.5 C). This carbon coating has the added benefit of reducing charging effects when viewing the SiN grids in the SEM/FIB.

Another option for seeding cells when one desires more control over their localization is to seed them on micropatterns. To test if SiN could be patterned, control SiN grids were

51
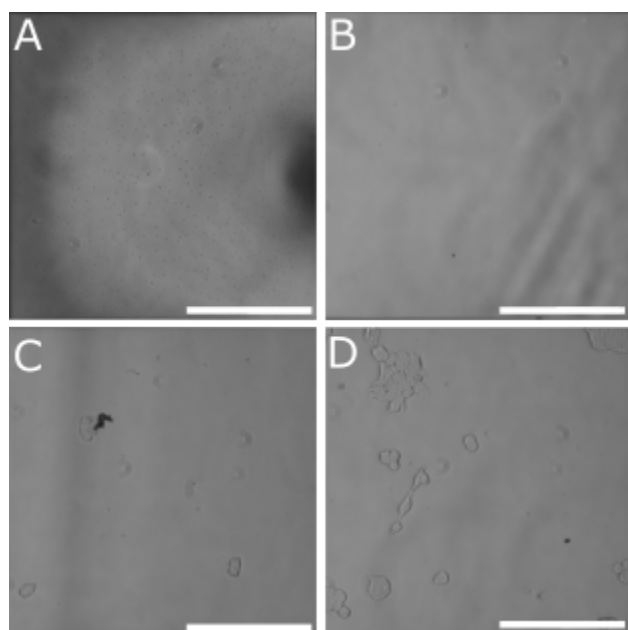
**Figure 3.5.** Silicon Nitride Surface Treatments for Cell Adhesion. (A) Silicon nitride grid window that has received no surface treatment. (B) Silicon nitride grid window that has been glow discharged and coated with fibronectin; (C) Silicon nitride grid window that has been coated with amorphous carbon and (D)Silicon nitride grid window that has been coated with amorphous carbon followed by incubation in fibronectin solution. All grids were incubated in the same solution of trypsinized NIH-3T3 cells and given 12 hours to allow cell adhesion. Scale bar = 200 $\mu$m
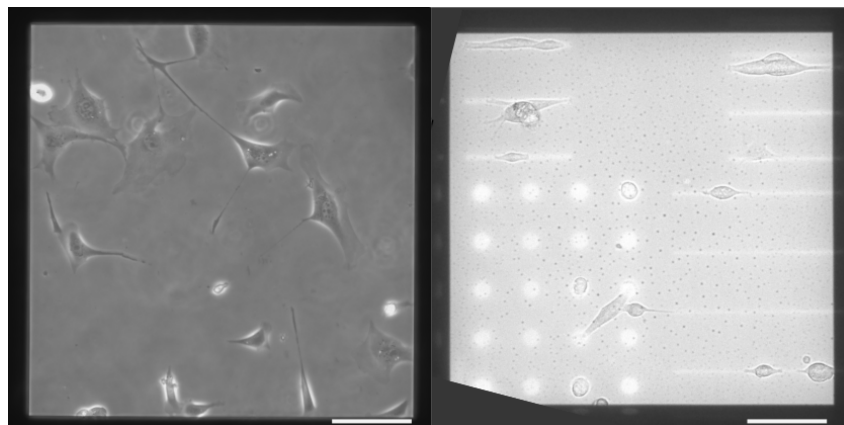
**Figure 3.6.** Cell culture on patterned vs non-patterned silicon nitride grids. Left: cells cultured on a grid where the whole window had been functionalized with fibronectin. Right: a patterned silicon nitride grid with cells adhering only to the patterned areas, identifiable by the increased fluorescent signal. Scale bars = $100\,\mu$m.

prepared in the standard manner described in the methods section, with glow discharge followed by incubation in fibronectin solution for one hour. Test grids were micropatterned as described in the methods with a variety of different shapes to see how the cells responded (Figure 3.6). Fibrinogen-AlexaFluor488 was used to visualize the patterns on the grid.

After allowing cells sufficient time to adhere to the grids, typically between 4-16 hours, the samples are plunge frozen using the previously described air drying rig. For pre-freeze drying, the level of drying of cells was controlled by regulating the air pressure of the nozzle and the speed with which it passed over the grid. Excessive pressure or too slow a drop rate causes overdrying, while using too little pressure, to fast a drop rate, or misplacing the grid within the air current, lead to underdried grids with large amounts of crystalline ice (Fig 3.7 A). When the air pressure was limited to 9 PSI at the last regulator and the nozzle dropped at a rate of 6 mm/sec, corresponding to approximately 0.5 sec of air passing over the grid, cells on the grid window were properly dried without desiccating (Fig 3.7 B).
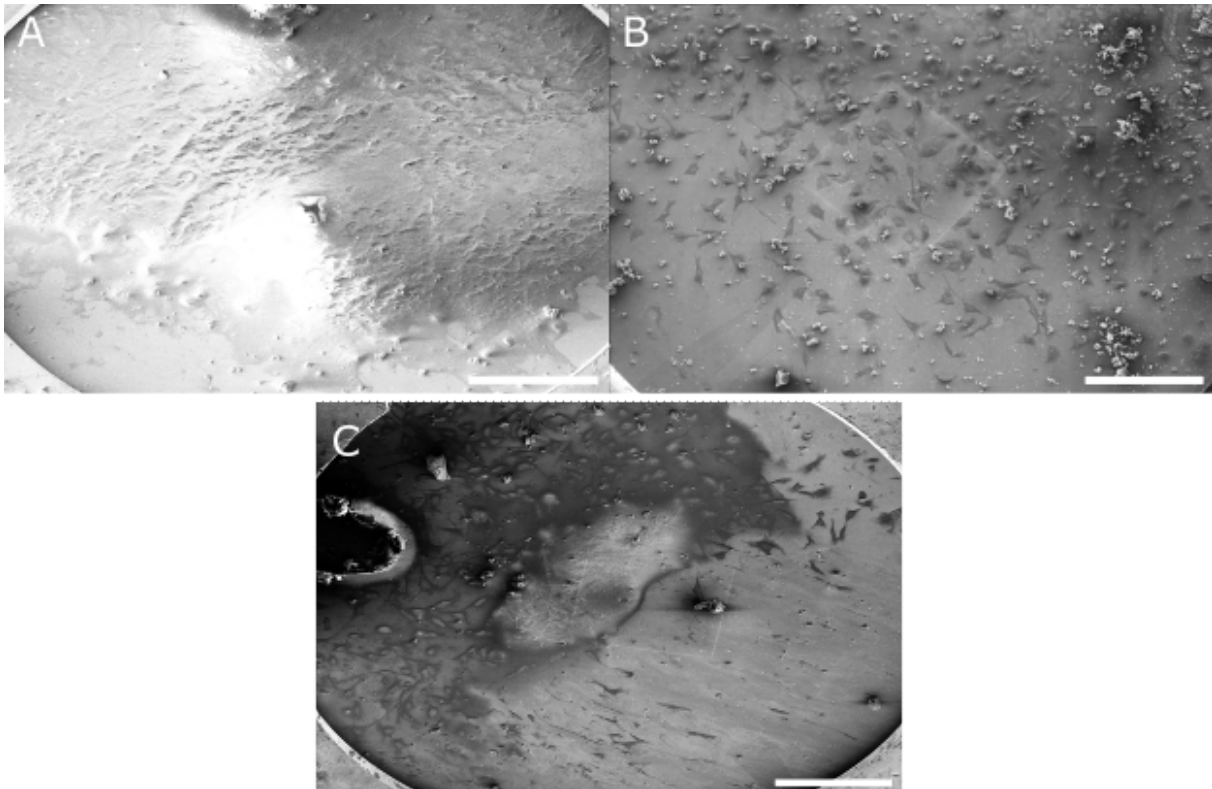
**Figure 3.7.** Drying Cells on Silicon Nitride Grids. (A) SEM view of an underdried SiN grid. (B) SEM view of a properly dried SiN grid. (C) Shows a grid with uneven drying, and severely dessicated cells in the upper right of the image. Scale bar = 400 $\mu$m.
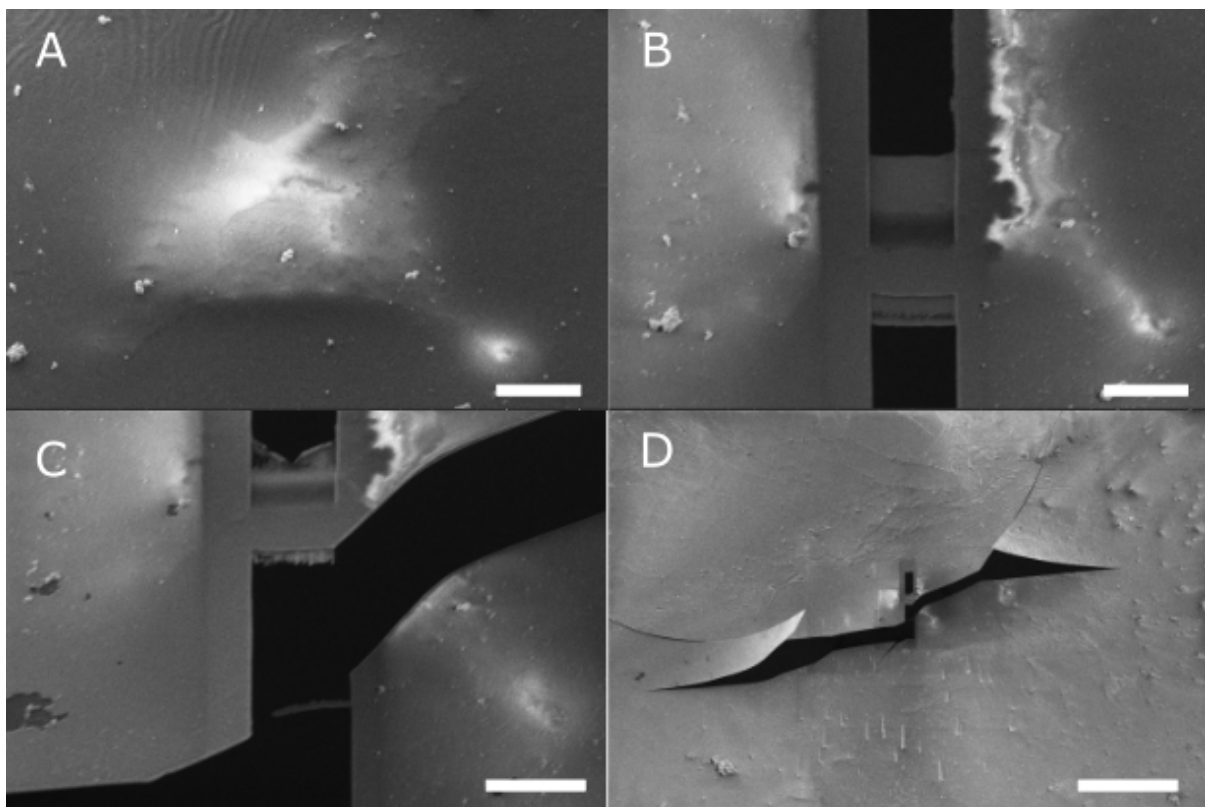
**Figure 3.8.** FIB Milling Cell on Silicon Nitride Grid. (A) Frozen cell being targeted for milling. (B) Cell after initial coarse milling. (C) Separation of membrane indicating rupture. (D) Lower magnification image of ruptured membrane. A-C scale bars = 10 $\mu$m. D scale bar = 100 $\mu$m.

### 3.3.2   FIB Milling

Cells grown on SiN grids were clearly identifiable by SEM (Fig 3.8 A). Once identified, cells would be FIB milled using the same parameters as carbon grids (Fig 3.8 B) [88]. However, because the process of FIB milling weakens the SiN membrane, the grids could not withstand milling without catastrophic failure in the vast majority of cases (Fig 3.8 C,D).

### 3.3.3   Conductive Coatings

The most probable cause of of membrane rupture is charge buildup resulting from the process of FIB milling [89]. Thus, we reasoned that a conductive coating should dissipate that charge. We began by testing if a conductive coating would prevent breakage on a bare grid with no ice or cells. A grid was sputter coated with iridium using an Emitech K575X Sputter Coater

for one cycle (30sec) for a target thickness of 5 nm, and loaded into an FEI Scios dual beam

FIB/SEM microscope cooled to -195°C, along with a non-coated control grid (Fig 3.9 A). The

non-coated grid was milled until membrane rupture, which occured during the milling of the

seventh lamella (Fig 3.9 B). Next, the iridium coated grid (Fig 3.9 C) was milled up to twenty

lamella (Fig 3.9 D).
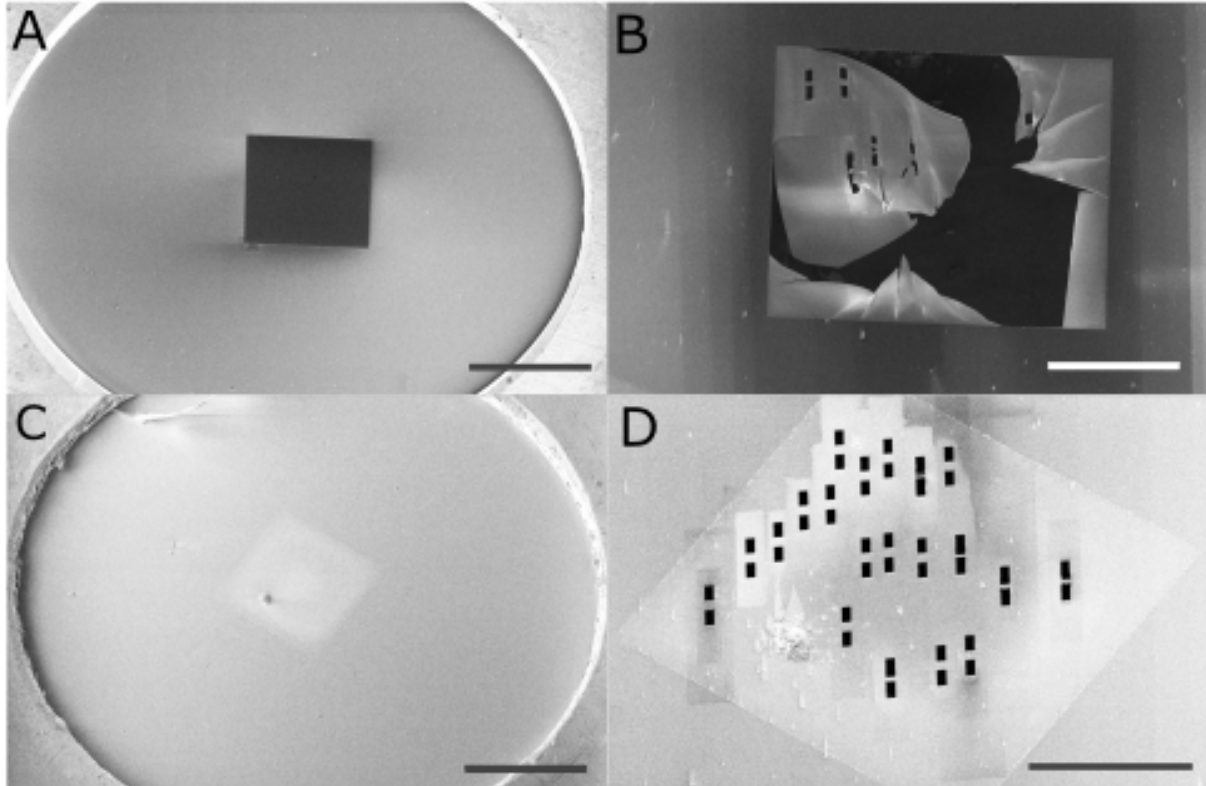


**Figure 3.9.** Focused Ion Beam Milling of Bare and Iridium Coated Silicon Nitride Grids. (A)
Overview SEM image of a bare, non-coated SiN grid. (B) Ruptured SiN membrane after milling
of the non-coated grid. (C) Overview SEM view of an iridium coated SiN grid. (D) Iridium
coated grid after milling of 20 lamellae. (A,C) scale bars = 500 $\mu$m. (B,D) scale bars = 200 $\mu$m.

Having shown that a conductive coating can prevent membrane rupture on bare grids, we

proceeded to testing if this effect held on grids holding frozen cells. Given that iridium is not a

material on which cells are regularly grown, we switched to a gold sputter coating instead, due

to its known lack of cytotoxicity. Grids were sputter coated in a Denton Discovery 18 Sputter

System with a gold target with a sputter time of 5 seconds for an approximate thickness of

5 nm. They were subsequently seeded with NIH-3T3 fibroblasts, which were allowed to adhere overnight, at which point the grids were dried using the air-drying apparatus and flash frozen. Cells appear to have grown normally on the gold coated grids (Fig 3.10 A). However, the gold coating did not prevent membrane rupture (Fig 3.10 B). Given the complexity of the gold coating procedure and the limited number of coated grids, no gold only sample was tested, as we inferred from the iridium results that conductive coatings prevent breakage on grids without cells.
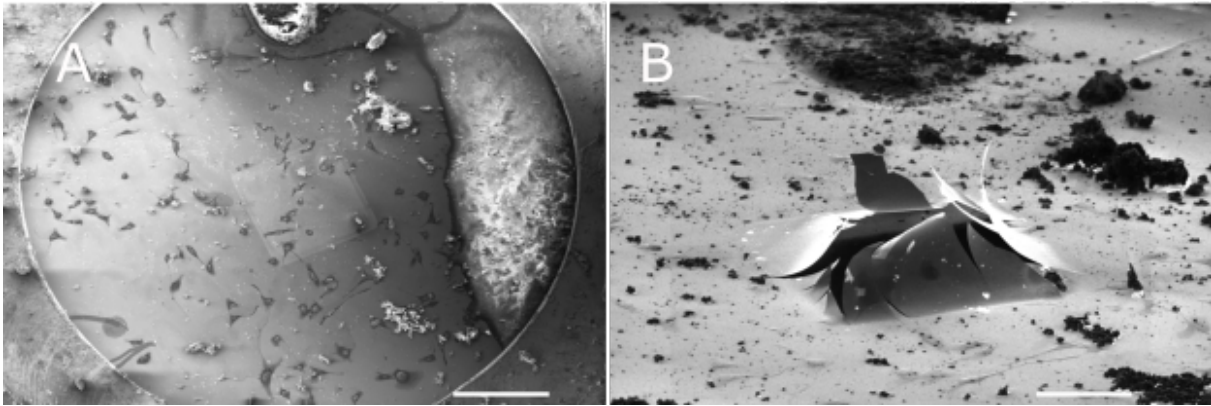


**Figure 3.10.** Focused Ion Beam Milling of Cells on Gold Coated Silicon Nitride Grids. (A) Overview SEM image of a gold-coated SiN grid with frozen cells. (B) Ruptured SiN membrane after milling of the gold-coated grid. Scale bars = 400 $\mu$m

### 3.3.4   Increased Membrane Thickness

Given the tendency of SiN to rupture during FIB milling, and given that conductive coatings did not prevent this rupture, we opted to increase the thickness of the SiN membrane to 200 nm (2spi custom order catalog no 9999902, 500x500 $\mu$m window, 100 nm support frame). These were prepared and processed in the same manner as the 100 nm thick membrane grids prior to FIB milling. However, as with the thinner membrane grids, the thicker grids would still rupture in the vast majority of cases (Fig 3.11). Increasing this thickness to 500 nm also did not prevent breakage.
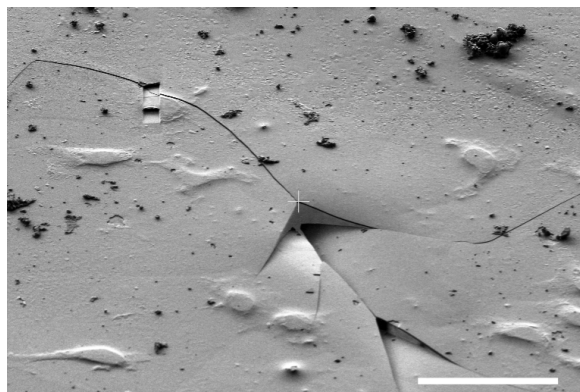
**Figure 3.11.** 200 nm thick SiN membrane ruptured by FIB milling. Scale bar = 100 $\mu$m.

## 3.4   Discussion

Here we have shown our efforts in adapting silicon nitride TEM grids as a potential platform for cryo-FIB-ET. First, we have demonstrated that cells can be grown on SiN grids with minimal surface treatment, and their morphology is indistinguishable from those cells grown on glass coverslips. This in itself is unsurprising, and should hold true for a range of different materials with mechanical properties similar to glass. This means that the grid handling techniques and the methods of attaching cells to SiN grids should be applicable to any other similar substrate.

We have also shown that by using a custom drying device we can remove enough liquid from the grids for the cells to vitrify, without dehydrating the cells. The cells frozen using this device show hydrated morphology and low levels of surrounding ice, indicating proper freezing. The methods developed here should be universally applicable to any non-porous substrate that cannot be dried by conventional means such as blotting. If such a substrate were also able to withstand FIB milling, these same methods developed for drying and freezing SiN grids would be directly transferable. However, since but the vitrified cells can not be cryo-FIB milled on SiN without catastrophic failure of the grid membrane, samples grown on SiN that require thinning cannot be viewed on a TEM in the same manner as quantifoil grids.

SiN grids may still present useful opportunities for controlling and imaging cellular

structures in thin regions that do not require FIB milling. Still, even though we were able to avoid any artifacts that may arise from growing cells on the irregular surface presented by quantifoil grids by utilizing SiN grids, we conclude that membrane failure prevents SiN grids from being a viable alternative platform for cryo-FIB-ET.

# Chapter 4

# Toward Correlative Light and Electron Microscopy of the Linker of the Nucleoskeleton and Cytoskeleton (LINC) Complex

## 4.1   Introduction

In order to function properly, all cells must integrate and respond to a wide variety of biochemical and mechanical inputs. For the mechanical inputs, cells must convert the forces they are subjected to into a biochemical signal in order to respond, in a process referred to as mechanotransduction [90]. One key component in cellular mechanotransduction is the linker of the nucleoskeleton to cytoskeleton (LINC) complex. The LINC complex is a multi-protein complex that spans both lipid bilayers of the nuclear envelope (NE), attaching to lamins and chromatin at the inner nuclear membrane (INM), reaching through the lumen of the NE and outer nuclear membrane (ONM) and connecting to cytoskeletal elements in the cytosol (Figure 4.1)[91]. At the INM, a complex of SUN domain proteins that interact with lamins at the nuclear cortex and span the INM reaching out into the lumen of the NE. In the lumen of the NE, the SUN domain proteins interact with KASH domains, another set of transmembrane proteins in ONM. KASH domain proteins in turn span the ONM, and connect to cytoskeletal elements either directly, as in the case of actin, or indirectly through interactions with kinesin, as in the case
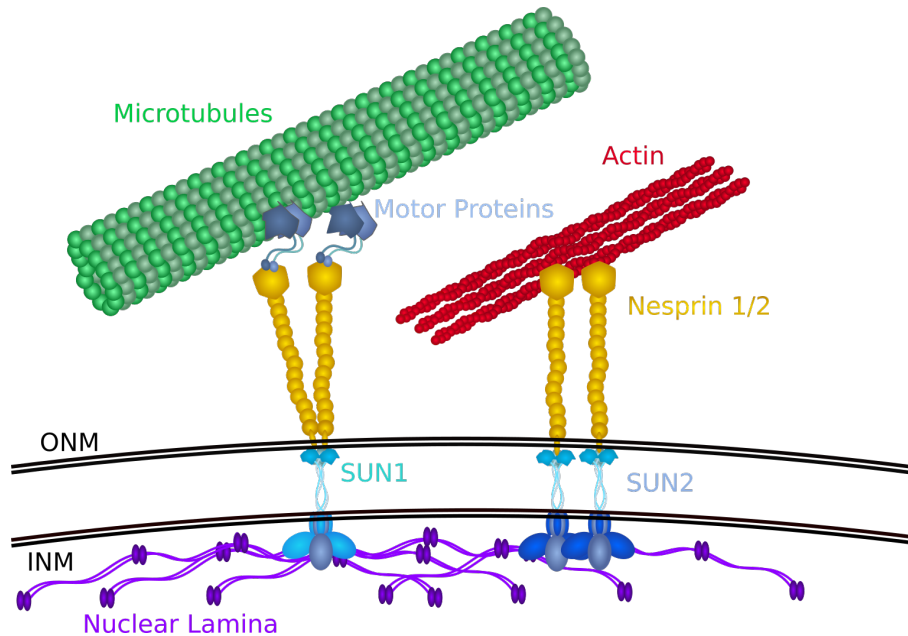
**Figure 4.1.** Linker of Nucleoskeleton to Cytoskeleton Complex.

of microtubules [92]. The LINC complex is critical for proper nuclear positioning within the cell, as well as anchoring chromatin to the nuclear membrane [93, 94], and mutations of LINC components are associated with a number of genetic diseases in humans [95].

Given the multiple roles of the LINC complex in the cell, as well as its significance in human disease, a structural understanding of the complex is needed. However, the complex has several features that make the structure difficult to determine by techniques relying on *in vitro* reconstitution. First, the LINC complex has many components with an ill-defined stoichiometry. Second, membrane proteins have long been challenging to reconstitute, and the LINC complex spans two separate membranes. The severe challenges posed by reconstituting the LINC complex mean cryo-ET is uniquely positioned to solve the complete structure compared to other approaches. Still, cryo-ET of the LINC complex presents a number of challenges of its own.

Because cells have to be milled to 100-200 nm in order obtain the highest quality data, one needs to know where to target FIB beam. This is accomplished using correlative light and electron microscopy (CLEM). This is a process where samples are imaged in a cryo-fluorescence

microscope prior to FIB milling. The fluorescence images can then be used to tell where to mill. Recently, CLEM has enabled the determination of the complete structure of LRRK2, marking the first time a structure has been solved *in situ* before it has been solved *in vitro* [39]. For the reasons stated above, the LINC complex is an even more difficult structure to determine *in vitro* than LRRK2, and will similarly need to be solved *in situ*.

The biggest challenge with respect to CLEM and cryo-FIB-ET of the LINC complex is locating it with confidence, especially in the z-axis. Even if x and y are perfectly localized, one still must capture the feature within the 100 nm thickness of the lamella. Unfortunately, the cryo-fluorescence microscopes available are still diffraction limited to around 400-500 nm resolution [96, 97], approximately twice the thickness aimed for in a lamella [6]. This means one risks milling away the source of the fluorescence. It is also very difficult to confidently assign an identity to a molecule that is in an area of diffuse fluorescent signal. To most effectively target the LINC complex, we need to enrich LINC assemblies into a form that is inducible and distinct. In addition to needing a target for FIB milling, we need a large number of copies of LINC complexes in order to determine the structure through subtomogram analysis (STA). These linear arrays of LINC would help to maximize the number of LINC complexes in the resulting tomograms by clustering them together in a small volume. If we cannot reliably have multiple copies in a tomogram, an infeasibly high number of tomograms would be required to meaningfully determine the structure.

To overcome the challenge of concentrating and targeting LINC, our approach is first to develop a technique for enriching LINC in identifiable linear arrays. Due to the LINC complex's role in nuclear repositioning through connections to actin [98, 99], linear arrays of LINC can be formed if the nucleus if forced to reposition itself. Normally, such arrays can be induced using wound healing or scratch assays to stimulate cellular migration. As the cells prepare to migrate, the nucleus is repositioned via the connections through the LINC complex to rearward moving lines of actin, thereby providing a clear target [98]. However, the scratch assay is not feasable for cryo-FIB-ET due to the need for a layer of confluent cells, which would inhibit

vitrification, as discussed in chapter 3, and the fact that the physical disruption required to scratch the monolayer would also damage the grid holding the cells. While the former can be overcome with high-pressure freezing [100, 101, 102], this process dramatically reduces the throughput of the cryo-ET workflow and thus is best avoided when possible.

In order to induce LINC lines without scratch assays, one can use mechanical forces that result in nucleus repositioning, a process that results in LINC lines. The nucleus can be repositioned within the cell using centrifugation; as adherent cells spin, the nucleus moves in the direction of the centrifugal force. Once centrifugation stops, the nucleus is repositioned through similar lines as seen in the migration assays [99]. An alternative strategy involves constraining cells by micropatterning to particular geometries. Cells grown on high aspect ratio (i.e. 1:10) micropatterns have shown a tendency to form LINC lines along lateral actin cables [103]. In this section I describe ongoing work toward a strategy to induce easily identifiable arrays of LINC complex target them using CLEM.

## 4.2 Materials and Methods

### 4.2.1 Micropatterning

Glass coverslips and EM grids were prepared in the following manner. Samples were glow discharged in a PELCO easiGlow glow discharge system (Ted Pella) for 60 s at 0.2 mbar at 20 mA. After glow discharge, the samples were incubated for 1 hour in a solution of poly-l-lysine-g-PEG (0.1 mg/mL dissolved in PBS). The PLL-g-PEG was then removed by pipetting, and the samples were rinsed 5 times with fresh PBS. After the last PBS rinse, excess liquid0 was removed and the samples covered with PLPP photoinitiator. Samples were then exposed to patterned UV light ($\lambda$ = 375nm) for a total energy of 900 $\mu$Joules/mm$^2$ using the PRIMO micropatterning system (Alvéole) on a Nikon T$_i$2. After exposure, samples were again rinsed 3 times in PBS and stored under PBS until use.

### 4.2.2 Cell lines and Culture

These experiments use a line of NIH-3T3 mouse embryonic fibroblasts transduced with the p130-3 pMSCV EGFP-C4-mini-nesprin2G to stably express a fluorescent variant of nesprin-2G that lacks the spectrin repeats s 3-54 while retaining the functionality of the LINC complex (donated by the Gregg Gundersen Lab, Columbia) [104]. Nesprin-2G is the KASH domain protein that spans the the ONM and binds to actin filaments in the cytosol, and a fluorescent version will allow us to identify areas with high levels of LINC complex.

### 4.2.3 Grid Seeding

Cells were grown in Dulbecco's Modified Eagle's Medium (DMEM) supplemented with 10% fetal calf serum (FCS) to 80% confluence and detatched from the culture dish using 1 mL trypsin-EDTA. Once detatched, trypsinization was quenched with 9 mL of DMEM. Cell concentration was counted and the cells spun down for resuspension to 1e6 cells/mL. This was used to make a 1e5 cells/mL suspension, which was then added to a dish with the intended substrates (either glass or EM grids). The cells were allowed to adhere for between 4-16 hours prior to either fixation or plunge freezing, depending on the sample [6].

### 4.2.4 Centrifugation

To test if LINC lines could be induced through centrifugation, a custom holder was designed to hold coverslips with cells in warm media (Figure 4.2). The holder is designed so that the bottom fits into a 50 mL conical. The bottom has holes so that liquid can pass through when inserting or removing the holder, and has slots for holding four coverslips. Finally, it has a handle so that on can easily take it in and out of the tube. The device is 3D printed using PLA+ ($e$SUN) with a hot-end temperature $220^oC$ and a plate temperature of $60^oC$. The holder should be printed at 100% infill so that it will sink.

For centrifugation, centrifuge with a swinging bucket rotor equipped to hold 50 mL conical tubes was preheated to $37^oC$. Glass coverslips with adhered cells were removed from
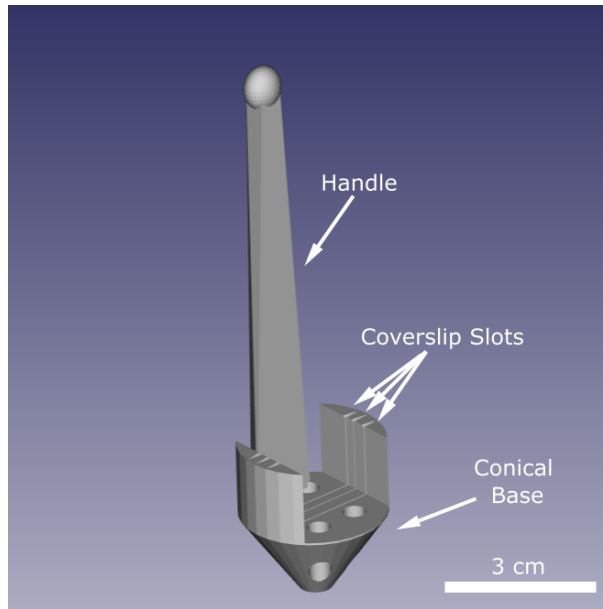
**Figure 4.2.** Holder for Centrifugation of Coverslips.

their culture dish up to 4 at a time and placed into the holder in a 50 mL conical tube with prewarmed DMEM. The tube was quickly weighed, and a corresponding balance tube measured out. Cells were centrifuged at 4000 x RCF for 30 minutes. The coverslips were then left in the warm media until the intended fixation timepoint.

Eventually this technique will need to be adapted to EM grids. To that end, a prototype another prototype holder was designed for holding EM grids. Like the version for the coverslips, the bottom is shaped to fit in a conical tube, but in in this case a 15 mL conical tube. It also has holes in the base to allow liquid to pass through when inserting into or removing it from the media. There are four parts to the design, the cartridge, the lid, the base, and the clamp (Figure 4.3). The cartridge has eight 3 mm wells for holding grids. The lid has a fits into the wells, and press the grids into place. The faces of the lid that press against the grids are concave to ensure only the edges of the grids are touched. Once the lid and the cartridge are assembled, the shorter end is stuck into the conical base, and the clamp is slid down the top being held in place by friction and keeping the assembly together.
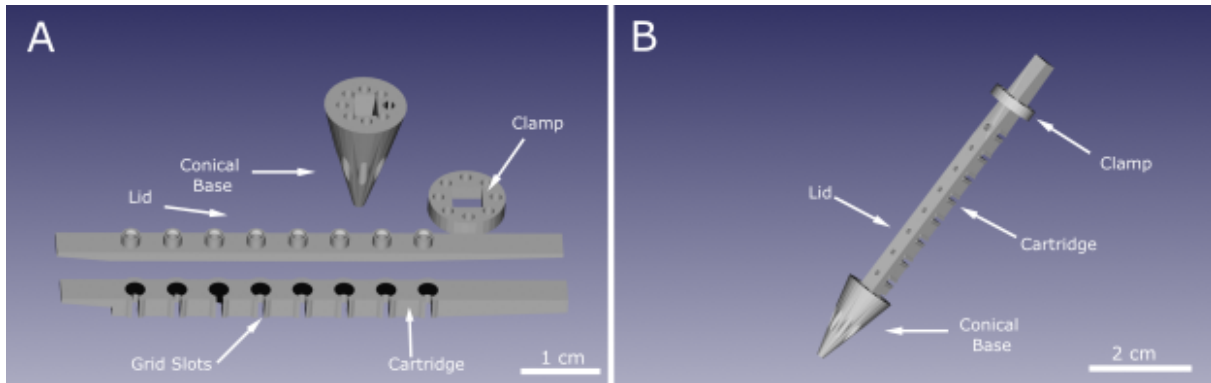
**Figure 4.3.** Holder for Centrifugation of Grids. (A) Disassembled grid centrifugation device. The lid fits over the cartridge, holding grids in the cartidge wells. The assembled lid-cartridge is inserted into the conical base, and the clamp slid down the wedge formed by the lid-cartridge. (B) The fully assembled centrifugation device.

### 4.2.5 Cell Staining and Fluorescence Microscopy

Coverslips were removed from media and fixed in 3% formaldehyde solution in PBS for 15 minutes. Samples were then rinsed 3 times with PBS with 0.1% Triton X-100, followed by 3 rinses with PBS. For samples where actin staining was desired, samples were then incubated in PBS with 1% BSA, 1x phalloidin-iFluor 488, at room temperature for 1 hour. After staining, samples were again rinsed 5 times in PBS and mounted on slides with mounting medium. Fixed samples were imaged with either a 20x / 0.75 plan apo air or 60x / 1.40 plan apo oil objective on a Nikon Ti2 using a Yokogawa-X1 spinning disk confocal system with a Photometrics Prime 95B back-thinned CMOS camera.

### 4.2.6 Cryo-Fluorescence Microscopy

The cryo stage of the SP8 (Lieca) was cooled to -195$^o$C, and LN$_2$ added to the transfer shuttle to cool. Clipped samples were loaded into the insertion catridge and the cartridge was transferred to the pre-cooled stage. A tiled series widefield overview was collected for both GFP and transmitted light. Cells of interest were imaged in scanning confocal mode. All images were acquired with a Leica HCX 50x / 0.90 plan apo CLEM air objective.

### 4.2.7 FIB milling

Frozen samples were loaded onto the pre-chilled ($190^o$C) stage of an Aquilos Dual Beam FIB/SEM (Thermo Fisher). The FIB milling procedure is described in detail in [6]. Briefly, a series lower magnification SEM images are collected in a tile series and stitched to provide an overview of the whole grid. From this, cells are selected for milling based on morphology and ice quality. Samples with a fluorescence overview map would use the fluorescence data as well to select targets. The sample is coated with an organometallic compound using a gas injection system (GIS). GIS deposition was continued for 30 seconds, at which point the GIS is removed from the microscope chamber. For each lamella, cells are machined in three stages: rough milling, with a beam current of 50 nA; intermediate milling, accelertion voltge of 100 pA; and fine milling, at 30 pA. Once all lamellae have undergone fine milling, a final polishing step at 10 pA is used to reduce contamination on the lamella surface. The samples are then transferred back to their holders under vacuum and stored in $LN_2$.

### 4.2.8 Cryo-Electron Tomography

Milled samples were loaded into a Titan Krios autoloader cassette (Thermo Fisher) under $LN_2$ and the cassette inserted into the autoloader. From the autoloader, a grid is selected and loaded onto the stage of the microscope. Dose-symmetric tilt series [105] were acquired from $\pm$ $48^o$ in $3^o$ increments with a $10^o$ pre-tilt. The micrographs were taken at a pixel size of 2.2Åwith a target defocus of -3 $\mu$m and a total dose 120e/Å$^2$. Motion correction and CTF correction were performed in Warp [27]. Tilt series were aligned and reconstructed by back projection in IMOD [44].
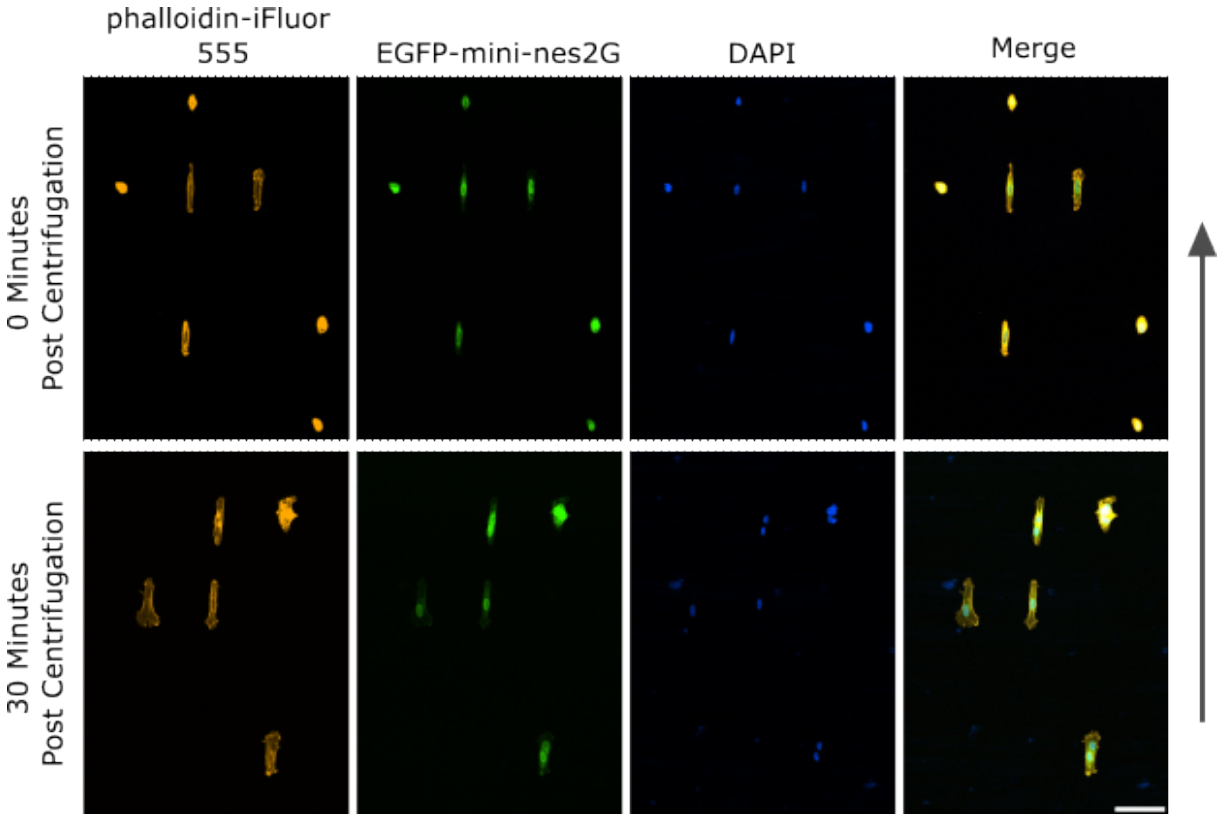
**Figure 4.4.** Centrifuged Patterned Cells. Patterned arrays of cells fixed immediately post centrifugation (left) and 30 minutes post centrifugation (right). Cells expressing mini-Nes2G-eGFP (green), actin stained with phalloidin-iFluor488 (orange) and DNA stained with DAPI (blue) . Black arrow on the right indicates direction of centrifugal force. Scale bars = $100\mu$m.

## 4.3 Results

### 4.3.1 Centrifugation

As explained above, one option for inducing LINC-mediated nuclear migration is through centrifugation [99]. By centrifuging cells, the nucleus moves in the direction of the centrifugal force, requiring the cell to reposition the nucleus. We aim to induce similar lines to those seen in the scratch assays by applying this technique to glass, to test, and eventually to grids.

To test the principle on glass, a custom device was designed to centrifuge cells coverslips 4.2. The device fit inside a 50 mL conical tube, and holds coverslips so that they are in line with the direction of centrifugal force. Cells were grown overnight on 10x100 $\mu$m micropatterns
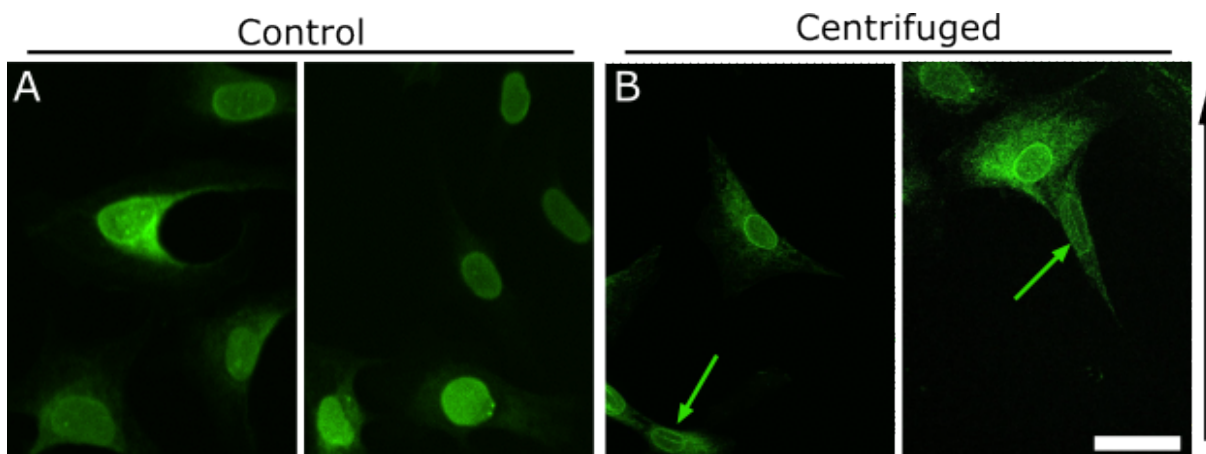
**Figure 4.5.** Representative cells with and without centrifugation. (A) Control cells expressing mini-Nes2G-eGFP that have not undergone centrifugation. (B) Cells expressing mini-Nes2G-eGFP fixed immediately post-centrifugation. Black arrow on the right indicates direction of centrifugal force. Scale bar = 100 $\mu$m.

before being centrifuged in a swinging bucket rotor. After centrifugation at 4000 x RCF for 30 minutes, cells were fixed at 0 and 30 minutes post centrifugation. In patterned and centrifuged cells, no strong difference was apparent in the nuclear positioning between the 0 and 30 minute timepoint (Figure 4.4).

While the difference in nuclear positioning between the centrifuged and the recovered cells was minimal, distinct lines of mini-Nes2G-eGFP were noticeably more common in cells post centrifugation compared to control.

To confirm that this technique would be viable on cryo-EM grids, grids were prepared in a similar manner to the glass coverslips. Once cells had adhered to the grids, the grids were transferred to the grid centrifugation device (Figure 4.3 and spun at 4000 x rcf. Using this assembly, grids could be centrifuged without unacceptable levels of damage, proving they can survive the centrifugation (Figure 4.6).

## 4.3.2 Patterning Cells on Grids

In order to ensure cells adhere to an area accessible to TEM (i.e. not on a grid bar), we employed a surface micropatterning technique know as LIMAP [76, 106]. As mentioned earlier,
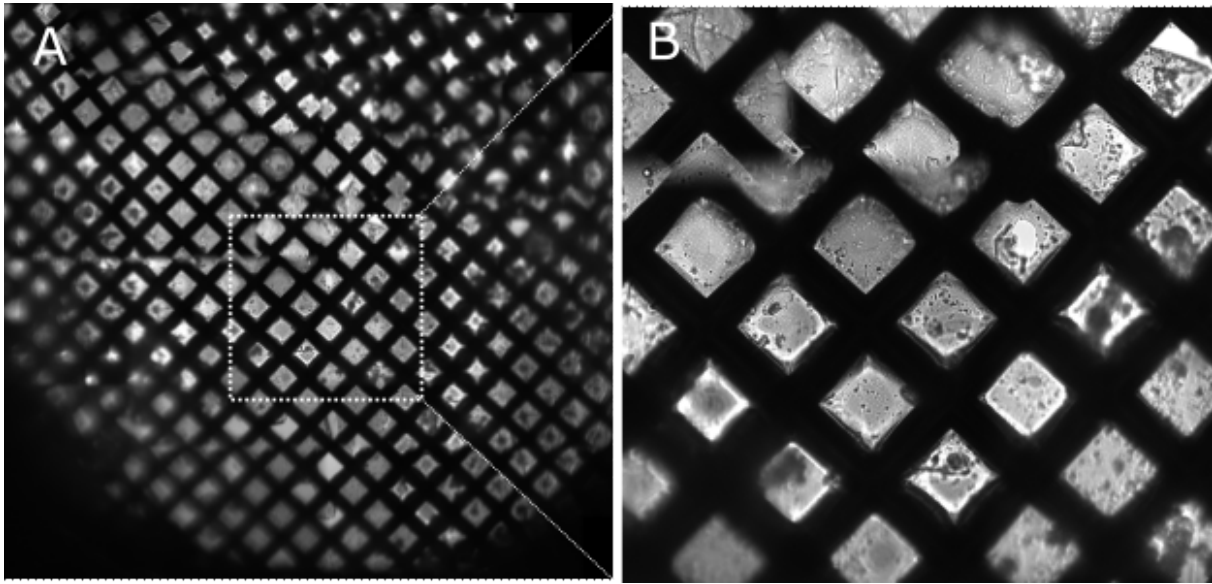
**Figure 4.6.** Stitched overview of a grid that has undergone centrifugation and plunge freezing. (A) Overview of the grid after centrifugation and plunge freezing. (B) Up close view of grid squares highlighted by the box in (A). The grid squares are largely intact.

patterns can also be used to enrich for certain structures of interest [99]. Grids were patterned such that a thin ($10\mu$m) line spanned the diagonal of each grid square. This ensured the cells were of maximum length and constrained to a shape known to induce LINC-associated actin lines (Figure 4.8 A,B)[103]. This orientation also lets one align the cells to the FIB beam by aligning the mesh of the grid with the milling slot on the autogrid, resulting in the long axis of the cells oriented $45^o$ relative to the FIB (Figure 4.7 A). Cryo-preserved cells that are constrained in this shape and orientation show clusters of mini-Nes2G-eGFP around the nucleus that would be targetable by CLEM (Figure 4.8 C).

### 4.3.3 Tomography

While we have yet not been able to confidently correlate a fluorescent signal with an apparent LINC complex in a tomogram, we have been collecting data around the NE in cells that have been grown on $50\,\mu$m circular micropatterns intended to keep the cells off of grid bars. What we expect to see for the LINC complex would be a series of densities spanning both the INM and the ONM, and extending out into the cytosol, ideally connecting to some

70
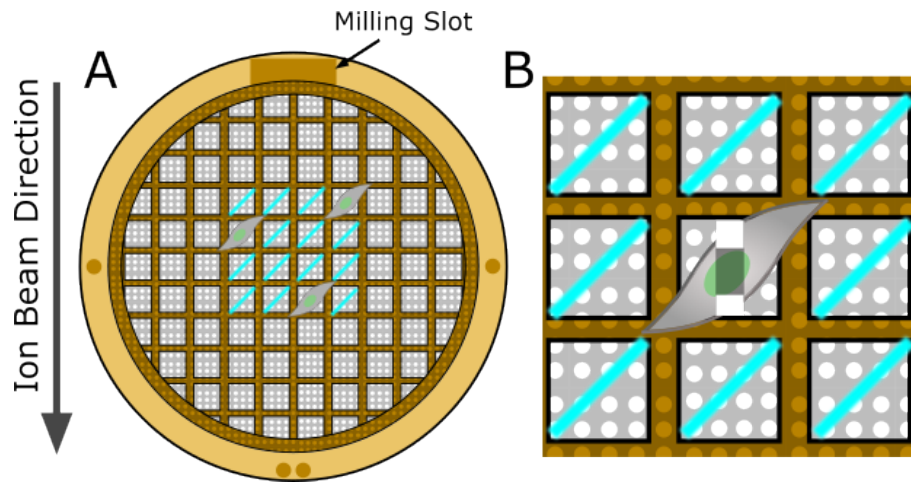
**Figure 4.7.** Cell Orientation with Respect to the FIB. (A) Overview demonstrating cell orientation relative to the FIB when patterned across the grid square diagonal. Cyan lines represent patterns with no cells attached. (B) Schematic of cell with a lamella milled through the nucleus.
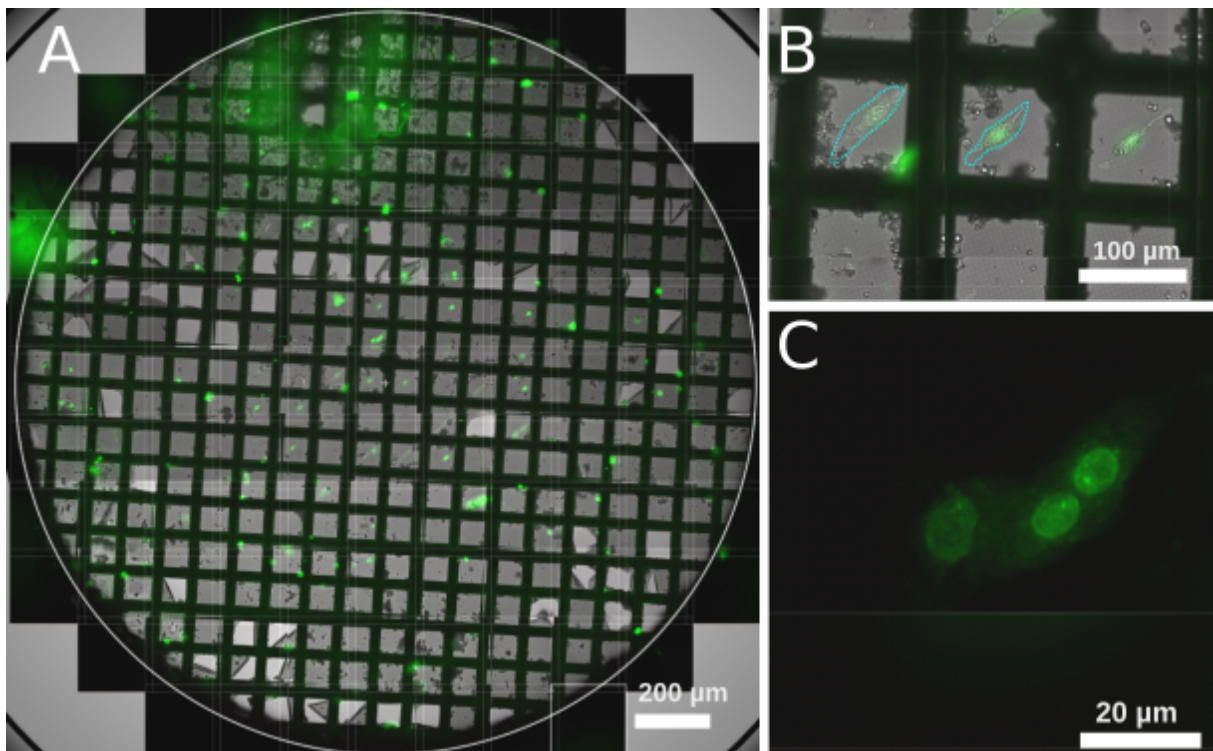


**Figure 4.8.** Cryo-fluorescence imaging of patterned cells. (A) Overview map of cryo-preserved cells patterned on an EM grid. (B) Micropatterned cells spanning grid square diagonal. Two cells highlighted with dashed green lines. (C) GFP signal from patterned cells on the grid.
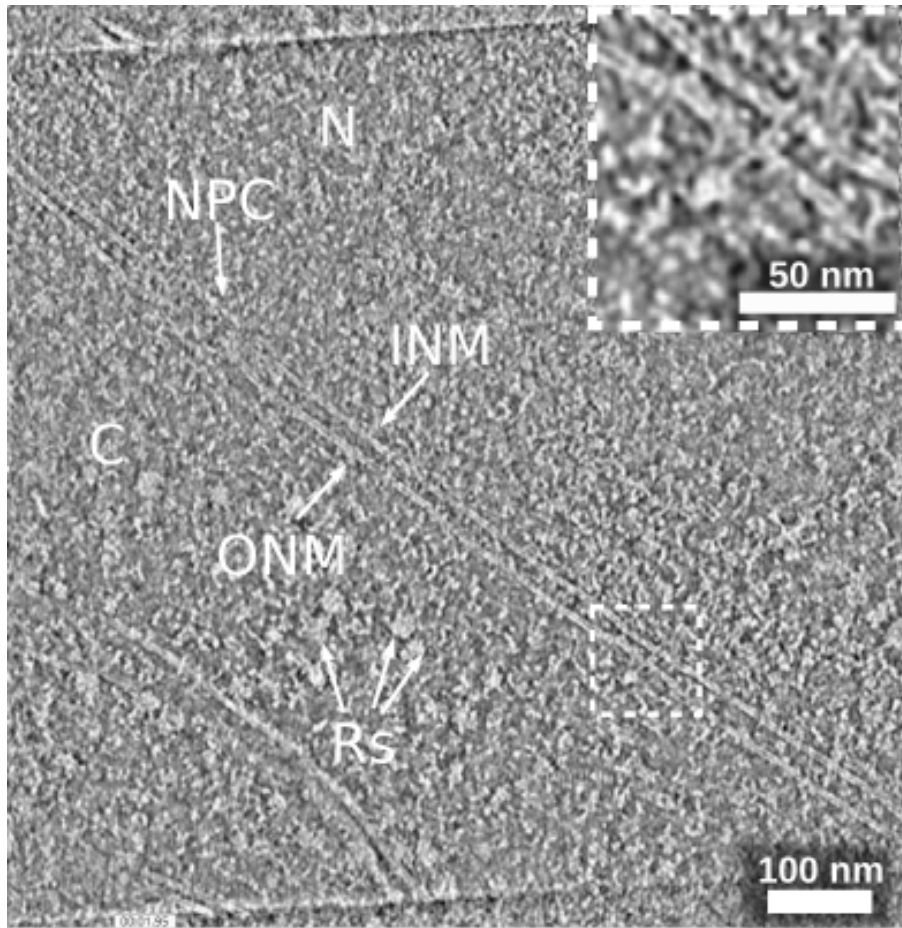
**Figure 4.9.** Tomogram of the Nuclear Envelope. 1 nm slice of a tomogram of the nuclear periphery. N:nucleus, C:cytoplasm, ONM:outer nuclear membrane, INM:inner nuclear membrane, Rs:ribosomes, NPC:nuclear pore complex. Inset showing the LINC-like density spanning the nuclear envelope.

sort of filamentous structure. After analyzing 14 tomograms of the nuclear envelope, only one

contained densities matching that description (Figure 4.9 A). As the inset clearly shows, there

is a continuous density starting at the inner leaf of the INM, spanning the lumen and ONM

and extending into the cytosol (Figure 4.9 B). This continuous filamentous density ends in a

globular portion. While we cannot say for sure that this is a LINC complex, it has the associated

characteristics.

## 4.4   Discussion

Here we have discussed strategies for targeting the LINC complex by CLEM and cryo-FIB-ET. As discussed, the primary challenges in this process are:

1. How to enrich LINC complex into targetable arrays.

2. How to target a given fluorescent signal by FIB milling without milling away the source of the fluorescence.

3. How to confidently associate fluorescent signal with a resolution of 200 nm to a putative LINC complex within a tomogram on the scale of 10s of nanometers.

So far, our work has focused primarily on this first aspect of enriching LINC complex arrays, which is a critical step before the next two problems can be addressed. Without mechanical stimuli, LINC complexes appear uniformly distributed in the nuclear envelope, showing a diffusely fluorescent signal throughout. Simply targetting the nuclear envelope (which is simple to do with cryo-FIB milling) does not capture areas enriched in LINC. It is also much more difficult to confirm that a diffuse fluorescent signal actually does correlate with a given structure in a tomogram, whereas the high contrast afforded by the LINC arrays could be much more confidently correlated with an observed LINC complex.

Centrifugation increased the occurrence of LINC lines, and may be a viable way of increasing their occurrence for CLEM samples. However, a remaining issue is the amount of grid handling the centrifugation protocol requires. While it may increase the likelihood of observing LINC lines, this tendency to damage the grids must be optimized to prevent a significant decline in the number of grids that survive through to imaging.

In our initial attempts, confined and elongated patterns did not reliably produce noticeable LINC lines when viewed by fluorescence. Current efforts focus on the actin stabilizing drug jasplakinolide, as increased stability of perinuclear actin cables can lead to an enrichment of LINC complex along the stabilized filaments [107].

Overall, we have made significant progress toward enriching LINC lines in a way that is compatible with the requirements of cryo-FIB-ET. Still, the samples will need to be optimized further. Currently, the low number of putative LINC complexes found in NE tomograms we have taken suggest we need to increase both the concentration of LINC in target areas and to automate high-througput cryo-FIB milling and tomography to successfully produce enough data to obtain a cryo-ET map that will unveil the molecular architecture of this elusive complex.

## 4.5   Supplementary Files

**Coverslip Centrifugation Holder**

.stl file format for slicing and 3D printing the coverslip holder.

**Grid Centrifugation Holder**

.stl file format for slicing and 3D printing the coverslip holder.

## 4.6   Acknowledgements

Most of the work in this chapter has been done in collaboration with Josh Hutchings, who will continue to expand on what has been shown here.

# Chapter 5

# Outlook

Cryo-FIB-ET is rife with opportunities and challenges for pushing the frontiers in cell biology. It offers unparalleled views of the cell interior, but is limited by sample damage and incomplete sampling. It has enabled complete structures to be determined entirely *in situ* [39], but the delicate substrates preclude many tools for manipulating cells traditionally available to cell biologist. Over the course of my doctoral research I have worked to address issues on both the experimental and data processing ends of cryo-FIB-ET.

To address the anisotropic distortions that tomograms suffer from, we applied a deconvolution approach that worked to incorporate both the CTF and the effects of back-projection into a synthetic PSF that was capable of completely restoring the missing wedge in simulated data, and partially in actual biological tomograms. This work, along with many other great tools emerging regularly, will help to improve the relevance of cryo-FIB-ET to cell biologists for whom missing wedge induced distortions may have been a deal breaker.

To address the issue of the substrates used in cryo-FIB-ET, we worked to characterize silicon nitride grids as a possible alternative. While we were able to adapt the workflow for preparing and plunge freezing to SiN grids, their tendency to break during FIB milling made them less attractive as an alternative. Still, the methods developed for handling and preparing SiN grids could easily be applicable to samples for which a large viewing window is needed, and which do not require FIB milling.

Finally, we looked into techniques for manipulating cells on grids to enrich for structures of interest such as the LINC complex. While we are still in the phase of determining the best targeting approach, preliminary data such as the centrifugation results suggest it is at least possible to enrich for LINC on grid. The work on this project will continue, hopefully building off of these findings.

The field of cryo-FIB-ET has expanded dramatically since this work began. Hopefully the work presented here will help continue that expansion and cement cryo-FIB-ET as the leading technique for *in situ* structural cell biology.

# Bibliography

[1] Elizabeth Villa et al. "Opening windows into the cell: focused-ion-beam milling for cryo-electron tomography". In: *Current Opinion in Structural Biology* 23.5 (2013), pp. 771–777. ISSN: 0959-440X. DOI: 10.1016/J.SBI.2013.08.006. URL: https://www.sciencedirect.com/science/article/pii/S0959440X13001589?via{\%}3Dihub.

[2] Michael Marko et al. "Focused-ion-beam thinning of frozen-hydrated biological specimens for cryo-electron microscopy". In: *Nature Methods* 4 (3 Mar. 2007), pp. 215–217. ISSN: 15487091. DOI: 10.1038/nmeth1014. URL: http://www.srim.org.

[3] Alexander Rigort et al. "Focused ion beam micromachining of eukaryotic cells for cryoelectron tomography". In: *Proceedings of the National Academy of Sciences of the United States of America* 109.12 (2012), pp. 4449–4454. ISSN: 00278424. DOI: 10.1073/pnas.1201333109.

[4] Jan Harapin et al. "Structural analysis of multicellular organisms with cryo-electron tomography". In: *Nature Methods* 12.7 (2015), pp. 634–636. ISSN: 1548-7091. DOI: 10.1038/nmeth.3401. URL: http://www.nature.com/articles/nmeth.3401.

[5] Miroslava Schaffer et al. "A cryo-FIB lift-out technique enables molecular-resolution cryo-ET within native Caenorhabditis elegans tissue". In: *Nature Methods* 16 (8 Aug. 2019), pp. 757–762. ISSN: 15487105. DOI: 10.1038/s41592-019-0497-5. URL: https://doi.org/10.1038/s41592-019-0497-5.

[6] Felix R. Wagner et al. "Preparing samples from whole cells using focused-ion-beam milling for cryo-electron tomography". In: *Nature Protocols 2020 15:6* 15 (6 May 2020), pp. 2041–2070. ISSN: 1750-2799. DOI: 10.1038/s41596-020-0320-x. URL: https://www.nature.com/articles/s41596-020-0320-x.

[7] Yi Wei Chang et al. "In Vivo Structures of the Helicobacter pylori cag Type IV Secretion System". In: *Cell Reports* 23 (3 Apr. 2018), pp. 673–681. ISSN: 22111247. DOI: 10.1016/j.celrep.2018.03.085. URL: https://pubmed.ncbi.nlm.nih.gov/29669273/.

[8] Vladan Lubit, Andrew Leis, and Wolfgang Baumeister. "Cryo-electron tomography of cells: connecting structure and function". In: *Histochem Cell Biol* 130 (2008), pp. 185–196. DOI: 10.1007/s00418-008-0459-y.

[9] Zunlong Ke et al. "Promotion of virus assembly and organization by the measles virus matrix protein". In: *Nature Communications* 9 (1 Dec. 2018), pp. 1–10. ISSN: 20411723. DOI: 10.1038/s41467-018-04058-2. URL: www.nature.com/naturecommunications.

[10] Joachim Frank. *Introduction: Principles of electron tomography*. Vol. 9780387690087. Springer New York, 2006, pp. 1–15. ISBN: 9780387690087. DOI: 10.1007/978-0-387-69008-7_1.

[11] John A.G. Briggs. "Structural biology in situ-the potential of subtomogram averaging". In: *Current Opinion in Structural Biology* 23 (2 Apr. 2013), pp. 261–267. ISSN: 0959440X. DOI: 10.1016/j.sbi.2013.02.003. URL: https://pubmed.ncbi.nlm.nih.gov/23466038/.

[12] Peijun Zhang. "Advances in cryo-electron tomography and subtomogram averaging and classification". In: *Current Opinion in Structural Biology* 58 (Oct. 2019), pp. 249–258. ISSN: 1879033X. DOI: 10.1016/j.sbi.2019.05.021.

[13] Jan Böhning and Tanmay A.M. Bharat. "Towards high-throughput in situ structural biology using electron cryotomography". In: *Progress in Biophysics and Molecular Biology* 160 (Mar. 2021), pp. 97–103. ISSN: 0079-6107. DOI: 10.1016/J.PBIOMOLBIO.2020.05.010.

[14] Joshua L. Dickerson et al. "Imaging biological macromolecules in thick specimens: The role of inelastic scattering in cryoEM". In: *Ultramicroscopy* 237 (July 2022), p. 113510. ISSN: 0304-3991. DOI: 10.1016/J.ULTRAMIC.2022.113510.

[15] Lindsay A. Baker and John L. Rubinstein. "Radiation damage in electron cryomicroscopy". In: *Methods in Enzymology* 481 (C 2010), pp. 371–388. ISSN: 00766879. DOI: 10.1016/S0076-6879(10)81015-8. URL: https://pubmed.ncbi.nlm.nih.gov/20887865/.

[16] Timothy Grant and Nikolaus Grigorieff. "Measuring the optimal exposure for single particle cryo-EM using a 2.6 Å reconstruction of rotavirus VP6". In: *eLife* 4 (MAY May 2015). DOI: 10.7554/ELIFE.06980.

[17] Hagen WJH, Wan W, and Briggs JAG. "Implementation of a cryo-electron tomography tilt-scheme optimized for high resolution subtomogram averaging". In: *Journal of structural biology* 197 (2 Feb. 2017), pp. 191–198. ISSN: 1095-8657. DOI: 10.1016/J.JSB.2016.06.007. URL: https://pubmed.ncbi.nlm.nih.gov/27313000/.

[18] Harold P. Erickson and A. Klug. "The Fourier Transform of an Electron Micrograph: Effects of Defocussing and Aberrations, and Implications for the Use of Underfocus Contrast Enhancement". In: *Berichte der Bunsengesellschaft für physikalische Chemie* 74 (11 Nov. 1970), pp. 1129–1137. ISSN: 0005-9021. DOI: 10.1002/BBPC.19700741109. URL: https://onlinelibrary.wiley.com/doi/full/10.1002/bbpc.19700741109https:

//onlinelibrary.wiley.com/doi/abs/10.1002/bbpc.19700741109https://onlinelibrary.wiley.com/doi/10.1002/bbpc.19700741109.

[19] H P Erickson and A Klug. "Measurement and compensation of defocusing and aberrations by Fourier processing of electron micrographs". In: *Philosophical Transactions of the Royal Society of London. B, Biological Sciences* 261 (837 May 1971), pp. 105–118. ISSN: 0080-4622. DOI: 10.1098/rstb.1971.0040. URL: https://royalsocietypublishing.org/.

[20] R. H. Wade. "A brief look at imaging and contrast transfer". In: *Ultramicroscopy* 46 (1-4 Oct. 1992), pp. 145–156. ISSN: 03043991. DOI: 10.1016/0304-3991(92)90011-8.

[21] Alexis Rohou and Nikolaus Grigorieff. "CTFFIND4: Fast and accurate defocus estimation from electron micrographs". In: *Journal of Structural Biology* 192 (2 Nov. 2015), pp. 216–221. ISSN: 10958657. DOI: 10.1016/j.jsb.2015.08.008.

[22] Martin Turk and Wolfgang Baumeister. "The promise and the challenges of cryo-electron tomography". In: *FEBS Letters* 594 (20 Oct. 2020), pp. 3243–3261. ISSN: 18733468. DOI: 10.1002/1873-3468.13948.

[23] Achilleas S. Frangakis and Reiner Hegerl. "Noise reduction in electron tomographic reconstructions using nonlinear anisotropic diffusion". In: *Journal of Structural Biology* 135 (3 2001), pp. 239–250. ISSN: 10478477. DOI: 10.1006/jsbi.2001.4406. URL: https://pubmed.ncbi.nlm.nih.gov/11722164/.

[24] José Jesús Fernández and Sam Li. "An improved algorithm for anisotropic nonlinear diffusion for denoising cryo-tomograms". In: *Journal of Structural Biology* 144 (1-2 2003), pp. 152–161. ISSN: 10478477. DOI: 10.1016/j.jsb.2003.09.010. URL: https://pubmed.ncbi.nlm.nih.gov/14643218/.

[25] Tim Oliver Buchholz et al. "Cryo-CARE: Content-aware image restoration for cryo-transmission electron microscopy data". In: vol. 2019-April. IEEE Computer Society, Apr. 2019, pp. 502–506. ISBN: 9781538636411. DOI: 10.1109/ISBI.2019.8759519.

[26] Xinrui Huang, Sha Li, and Song Gao. "Exploring an optimal wavelet-based filter for cryo-ET imaging". In: *Scientific Reports* 8 (1 Dec. 2018), p. 2582. ISSN: 20452322. DOI: 10.1038/s41598-018-20945-6. URL: www.nature.com/scientificreports/.

[27] Dimitry Tegunov and Patrick Cramer. "Real-time cryo-electron microscopy data preprocessing with Warp". In: *Nature Methods* 16 (11 Nov. 2019), pp. 1146–1152. ISSN: 15487105. DOI: 10.1038/s41592-019-0580-y.

[28] Robert P. Dougherty. "Extensions of DAMAS and benefits and limitations of deconvolution in beamforming". In: vol. 3. AIAA International, 2005, pp. 2036–2048. ISBN: 1563477300. DOI: 10.2514/6.2005-2961. URL: http://arc.aiaa.org.

[29]   Daniel Sage et al. "DeconvolutionLab2: An open-source software for deconvolution microscopy". In: *Methods* 115 (Feb. 2017), pp. 28–41. ISSN: 10959130. DOI: 10.1016/j.ymeth.2016.12.015. URL: https://pubmed.ncbi.nlm.nih.gov/28057586/.

[30]   Barnali Waugh et al. "Three-dimensional deconvolution processing for STEM cryotomography". In: *Proceedings of the National Academy of Sciences* 117 (44 Nov. 2020), pp. 27374–27380. ISSN: 0027-8424. DOI: 10.1073/PNAS.2000700117. URL: https://www.pnas.org/content/117/44/27374.

[31]   Tristan Bepler et al. "Topaz-Denoise: general deep denoising models for cryoEM and cryoET". In: *Nature Communications* 11 (1 Dec. 2020), pp. 1–12. ISSN: 20411723. DOI: 10.1038/s41467-020-18952-1. URL: https://doi.org/10.1038/s41467-020-18952-1.

[32]   Rui Yan et al. "MBIR: A cryo-ET 3D reconstruction method that effectively minimizes missing wedge artifacts and restores missing information". In: *Journal of Structural Biology* 206 (2 May 2019), pp. 183–192. ISSN: 10958657. DOI: 10.1016/j.jsb.2019.03.002. URL: https://pubmed.ncbi.nlm.nih.gov/30872095/.

[33]   Sarah Frisken Gibson and Frederick Lanni. "Experimental test of an analytical model of aberration in an oil-immersion objective lens used in three-dimensional light microscopy". In: *Journal of the Optical Society of America A* 9.1 (1992), p. 154. ISSN: 1084-7529. DOI: 10.1364/josaa.9.000154.

[34]   J Swedlow, J Sedat, and D Agard. "Deconvolution in optical microscopy". In: *Deconvolution of Images and Spectra, 2nd edition*. Ed. by P Jansson. 2nd. San Diego: Academic Press, 1997, pp. 284–309.

[35]   Z. Kam et al. "Computational adaptive optics for live three-dimensional biological imaging". In: *Proceedings of the National Academy of Sciences of the United States of America* 98.7 (2001), pp. 3790–3795. ISSN: 00278424. DOI: 10.1073/pnas.071275698.

[36]   P Jansson. *Deconvolution of images and spectra*. 2nd. New York: Academic Press, 1997. ISBN: ISBN-13:978-0-486-45325-5.

[37]   Muthuvel Arigovindan et al. "High-resolution restoration of 3D structures from widefield images with extreme low signal-to-noise-ratio". In: *Proceedings of the National Academy of Sciences of the United States of America* 110.43 (2013), pp. 17344–17349. ISSN: 00278424. DOI: 10.1073/pnas.1315675110.

[38]   Shoh Asano, Benjamin D. Engel, and Wolfgang Baumeister. "In Situ Cryo-Electron Tomography: A Post-Reductionist Approach to Structural Biology". In: *Journal of Molecular Biology* 428 (2 Jan. 2016), pp. 332–343. ISSN: 0022-2836. DOI: 10.1016/J.JMB.2015.09.030.

[39] R. Watanabe et al. "The In Situ Structure of Parkinson's Disease-Linked LRRK2". In: *Cell* 182.6 (2020), pp. 1508–1518.

[40] C. K. Deniston et al. "Structure of LRRK2 in Parkinson's disease and model for microtubule interaction". In: *Nature* (2020).

[41] Martin Schorb et al. "Software tools for automated transmission electron microscopy". In: *Nature Methods* 16 (6 June 2019), pp. 471–477. ISSN: 15487105. DOI: 10.1038/s41592-019-0396-9. URL: https://pubmed.ncbi.nlm.nih.gov/31086343/.

[42] W. J. H. Hagen, W. Wan, and J. A. G. Briggs. "Implementation of a cryo-electron tomography tilt-scheme optimized for high resolution subtomogram averaging". In: *J Struct Biol* 197.2 (Feb. 2017), pp. 191–198.

[43] S. Q. Zheng et al. "MotionCor2: anisotropic correction of beam-induced motion for improved cryo-electron microscopy". In: *Nat Methods* 14.4 (Apr. 2017), pp. 331–332.

[44] J. R. Kremer, D. N. Mastronarde, and J. R. McIntosh. "Computer visualization of three-dimensional image data using IMOD". In: *J Struct Biol* 116.1 (1996), pp. 71–76.

[45] Daniel Castaño-Díez et al. "Dynamo: A flexible, user-friendly development tool for subtomogram averaging of cryo-EM data in high-performance computing environments". In: *Journal of Structural Biology* (2012). ISSN: 10478477. DOI: 10.1016/j.jsb.2011.12.017.

[46] Shangyu Dang et al. "Cryo-EM structures of the TMEM16A calciumactivated chloride channel". In: *Nature* 552.7685 (2017), pp. 426–429. ISSN: 14764687. DOI: 10.1038/nature25024. URL: http://www.ncbi.nlm.nih.gov/pubmed/29236684http://www.pubmedcentral.nih.gov/articlerender.fcgi?artid=PMC5750132.

[47] Pettersen EF et al. "UCSF Chimera–a visualization system for exploratory research and analysis". In: *Journal of computational chemistry* 25 (13 Oct. 2004), pp. 1605–1612. ISSN: 0192-8651. DOI: 10.1002/JCC.20084. URL: https://pubmed.ncbi.nlm.nih.gov/15264254/.

[48] Tang G et al. "EMAN2: an extensible image processing suite for electron microscopy". In: *Journal of structural biology* 157 (1 Jan. 2007), pp. 38–46. ISSN: 1047-8477. DOI: 10.1016/J.JSB.2006.05.009. URL: https://pubmed.ncbi.nlm.nih.gov/16859925/.

[49] Sven R. Carlsson and Anne Simonsen. "Membrane dynamics in autophagosome biogenesis". In: *Journal of Cell Science* 128 (2 Jan. 2015), pp. 193–205. ISSN: 14779137. DOI: 10.1242/jcs.141036.

[50] H. Chen et al. "PRIISM: an integrated system for display and analysis of 3-D microscope images". In: ed. by Raj S. Acharya, Carol J. Cogswell, and Dmitry B. Goldgof. Vol. 1660.

SPIE, June 1992, pp. 784–790. DOI: 10.1117/12.59604. URL: http://proceedings.spiedigitallibrary.org/proceeding.aspx?articleid=987191.

[51]    Daniel Castaño-Díez and Giulia Zanetti. *In situ structure determination by subtomogram averaging*. 2019. DOI: 10.1016/j.sbi.2019.05.011. URL: https://pubmed.ncbi.nlm.nih.gov/31233977/.

[52]    Julia Mahamid et al. "Visualizing the molecular sociology at the HeLa cell nuclear periphery". In: *Science* 351 (6276 Feb. 2016), pp. 969–972. ISSN: 10959203. DOI: 10.1126/science.aad8857. URL: http://science.sciencemag.org/.

[53]    Joshua Hutchings et al. "Subtomogram averaging of COPII assemblies reveals how coat organization dictates membrane shape". In: *Nature Communications* 9 (1 Dec. 2018), pp. 1–8. ISSN: 20411723. DOI: 10.1038/s41467-018-06577-4. URL: www.nature.com/naturecommunications.

[54]    Maryam Khoshouei et al. "Subtomogram analysis using the Volta phase plate". In: *Journal of Structural Biology* 197 (2 Feb. 2017), pp. 94–101. ISSN: 10958657. DOI: 10.1016/j.jsb.2016.05.009.

[55]    Danielle A. Grotjahn et al. "Cryo-electron tomography reveals that dynactin recruits a team of dyneins for processive motility". In: *Nature Structural and Molecular Biology* 25.3 (2018), pp. 203–207. ISSN: 15459985. DOI: 10.1038/s41594-018-0027-7. URL: https://pubmed.ncbi.nlm.nih.gov/29416113/.

[56]    Zunlong Ke et al. "Structures and distributions of SARS-CoV-2 spike proteins on intact virions". In: *Nature* 588 (7838 Dec. 2020), pp. 498–502. ISSN: 14764687. DOI: 10.1038/s41586-020-2665-2. URL: https://doi.org/10.1038/s41586-020-2665-2.

[57]    Martin Obr and Florian K.M. Schur. "Structural analysis of pleomorphic and asymmetric viruses using cryo-electron tomography and subtomogram averaging". In: *Advances in Virus Research* 105 (Jan. 2019), pp. 117–159. ISSN: 15578399. DOI: 10.1016/bs.aivir.2019.07.008.

[58]    Cristina Jiménez-Ortigosa et al. "Preliminary structural elucidation of $\beta$-(1,3)-glucan synthase from candida glabrata using cryo-electron tomography". In: *Journal of Fungi* 7 (2 Feb. 2021), pp. 1–13. ISSN: 2309608X. DOI: 10.3390/jof7020120. URL: https://pubmed.ncbi.nlm.nih.gov/33562124/.

[59]    Josie L. Ferreira et al. "Gamma-proteobacteria eject their polar flagella under nutrient depletion, retaining flagellar motor relic structures". In: *PLoS Biology* 17 (3 Mar. 2019). ISSN: 15457885. DOI: 10.1371/journal.pbio.3000165. URL: https://pubmed.ncbi.nlm.nih.gov/30889173/.

[60] Beata Turoňová et al. "In situ structural analysis of SARS-CoV-2 spike reveals flexibility mediated by three hinges". In: *Science* 370 (6513 Oct. 2020), pp. 203–208. ISSN: 10959203. DOI: 10.1126/science.abd5223. URL: https://pubmed.ncbi.nlm.nih.gov/32817270/.

[61] Jianfeng Lin et al. "The structural heterogeneity of radial spokes in cilia and flagella is conserved". In: *Cytoskeleton* 69 (2 Feb. 2012), pp. 88–100. ISSN: 19493584. DOI: 10.1002/cm.21000. URL: https://pubmed.ncbi.nlm.nih.gov/22170736/.

[62] Yoshiyuki Fukuda et al. "In situ structural studies of tripeptidyl peptidase II (TPPII) reveal spatial association with proteasomes". In: *Proceedings of the National Academy of Sciences of the United States of America* 114 (17 Apr. 2017), pp. 4412–4417. ISSN: 10916490. DOI: 10.1073/pnas.1701367114. URL: /pmc/articles/PMC5410853//pmc/articles/PMC5410853/?report=abstracthttps://www.ncbi.nlm.nih.gov/pmc/articles/PMC5410853/.

[63] Shoh Asano et al. "A molecular census of 26S proteasomes in intact neurons". In: *Science* 347 (6220 Jan. 2015), pp. 439–442. ISSN: 10959203. DOI: 10.1126/science.1261197. URL: http://science.sciencemag.org/.

[64] Gregor L. Weiss et al. "Structure and Function of a Bacterial Gap Junction Analog". In: *Cell* 178 (2 July 2019), 374–384.e15. ISSN: 10974172. DOI: 10.1016/j.cell.2019.05.055. URL: https://pubmed.ncbi.nlm.nih.gov/31299201/.

[65] Benjamin A. Himes and Peijun Zhang. "emClarity: software for high-resolution cryo-electron tomography and subtomogram averaging". In: *Nature Methods* 15 (11 Nov. 2018), pp. 955–961. ISSN: 15487105. DOI: 10.1038/s41592-018-0167-z. URL: https://pubmed.ncbi.nlm.nih.gov/30349041/.

[66] Hstau Y. Liao and Joachim Frank. *Definition and Estimation of Resolution in Single-Particle Reconstructions*. 2010. DOI: 10.1016/j.str.2010.05.008.

[67] J W Goodman. *Introduction to Fourier Optics*. 2nd. New York: McGraw-Hill Companies, 1968, pp. 161–165. ISBN: 0-07-024254-2.

[68] Jong Chul Ye. "Compressed sensing MRI: a review from signal processing perspective". In: *BMC Biomedical Engineering* 1.1 (2019), pp. 1–17. ISSN: 2524-4426. DOI: 10.1186/s42490-019-0006-z.

[69] Rowan Leary et al. "Compressed sensing electron tomography". In: *Ultramicroscopy* 131 (2013), pp. 70–91. ISSN: 03043991. DOI: 10.1016/j.ultramic.2013.03.019.

[70] Vladan Lučić, Alexander Rigort, and Wolfgang Baumeister. "Cryo-electron tomography: The challenge of doing structural biology in situ". In: *Journal of Cell Biology* 202

(3 Aug. 2013), pp. 407–419. ISSN: 0021-9525. DOI: 10.1083/JCB.201304193. URL: www.jcb.org/cgi/doi/10.1083/jcb.201304193.

[71] Georg Wolff et al. "Mind the gap: Micro-expansion joints drastically decrease the bending of FIB-milled cryo-lamellae". In: *Journal of Structural Biology* 208 (3 Dec. 2019), p. 107389. ISSN: 1047-8477. DOI: 10.1016/J.JSB.2019.09.006.

[72] Joel Quispe et al. "An Improved Holey Carbon Film for Cryo-Electron Microscopy". In: (2007). DOI: 10.1017/S1431927607070791.

[73] Christopher J Russo and Lori A Passmore. "Progress towards an optimal specimen support for electron cryomicroscopy". In: *Current Opinion in Structural Biology* 37 (2016), pp. 81–89. ISSN: 0959-440X. DOI: 10.1016/J.SBI.2015.12.007. URL: https://www.sciencedirect.com/science/article/pii/S0959440X15001931.

[74] Yingnan Wu et al. "The Combined Effect of Substrate Stiffness and Surface Topography on Chondrogenic Differentiation of Mesenchymal Stem Cells." In: *Tissue engineering. Part A* 23.1-2 (2017), pp. 43–54. ISSN: 1937-335X. DOI: 10.1089/ten.TEA.2016.0123. URL: http://www.ncbi.nlm.nih.gov/pubmed/27824280.

[75] Andrew D Doyle et al. "One-dimensional topography underlies three-dimensional fibrillar cell migration." In: *The Journal of cell biology* 184.4 (2009), pp. 481–90. ISSN: 1540-8140. DOI: 10.1083/jcb.200810041. URL: http://www.ncbi.nlm.nih.gov/pubmed/19221195http://www.pubmedcentral.nih.gov/articlerender.fcgi?artid=PMC2654121.

[76] Pierre-Olivier Strale et al. "Multiprotein Printing by Light-Induced Molecular Adsorption". In: *Advanced Materials* 28.10 (2016), pp. 2024–2029. ISSN: 09359648. DOI: 10.1002/adma.201504154. URL: http://doi.wiley.com/10.1002/adma.201504154.

[77] Marc Schmutz et al. "Defects of planarity of carbon films supported on electron microscope grids revealed by reflected light microscopy". In: *Journal of Structural Biology* 112 (3 1994), pp. 252–258. ISSN: 10958657. DOI: 10.1006/JSBI.1994.1025.

[78] Marc Schmutz and Alain Brisson. "Analysis of carbon film planarity by reflection light microscopy". In: *Ultramicroscopy* 63 (3-4 July 1996), pp. 263–272. ISSN: 0304-3991. DOI: 10.1016/0304-3991(96)00044-7.

[79] Leonid A. Bendersky and Frank W. Gayle. "Electron Diffraction Using Transmission Electron Microscopy". In: *Journal of Research of the National Institute of Standards and Technology* 106 (6 2001), p. 997. ISSN: 1044677X. DOI: 10.6028/JRES.106.051. URL: /pmc/articles/PMC4865294//pmc/articles/PMC4865294/?report=abstracthttps://www.ncbi.nlm.nih.gov/pmc/articles/PMC4865294/.

[80] B. J. BATTERSBY et al. "Vitrification of aqueous suspensions from a controlled environment for electron microscopy: An improved plunge-cooling device". In: *Journal of*

*Microscopy* 176 (2 Nov. 1994), pp. 110–120. ISSN: 1365-2818. DOI: 10.1111/J.1365-2818.1994.TB03505.X. URL: https://onlinelibrary.wiley.com/doi/full/10.1111/j.1365-2818.1994.tb03505.xhttps://onlinelibrary.wiley.com/doi/abs/10.1111/j.1365-2818.1994.tb03505.xhttps://onlinelibrary.wiley.com/doi/10.1111/j.1365-2818.1994.tb03505.x.

[81] V. Lausch et al. "Silicon nitride grids are compatible with correlative negative staining electron microscopy and tip-enhanced Raman spectroscopy for use in the detection of micro-organisms". In: *Journal of Applied Microbiology* 116 (6 2014), pp. 1521–1530. ISSN: 13652672. DOI: 10.1111/JAM.12492.

[82] Rory Stine et al. "Formation of Primary Amines on Silicon Nitride Surfaces: a Direct, Plasma-Based Pathway to Functionalization". In: (2007). DOI: 10.1021/LA0635653. URL: https://pubs.acs.org/doi/abs/10.1021/la0635653.

[83] Yuriko Masuda et al. "Cell culture on hydrophilicity-controlled silicon nitride surfaces". In: *World Journal of Microbiology and Biotechnology* 31.12 (2015), pp. 1977–1982. ISSN: 0959-3993. DOI: 10.1007/s11274-015-1946-7. URL: http://link.springer.com/10.1007/s11274-015-1946-7.

[84] Frank L. Riley. "Silicon Nitride and Related Materials". In: *Journal of the American Ceramic Society* 83.2 (2004), pp. 245–265. ISSN: 00027820. DOI: 10.1111/j.1151-2916.2000.tb01182.x. URL: http://doi.wiley.com/10.1111/j.1151-2916.2000.tb01182.x.

[85] Johan Jaime Medina Benavente et al. "Evaluation of Silicon Nitride as a Substrate for Culture of PC12 Cells: An Interfacial Model for Functional Studies in Neurons". In: *PLoS ONE* 9.2 (2014). Ed. by Wilbur Lam, e90189. ISSN: 1932-6203. DOI: 10.1371/journal.pone.0090189. URL: http://www.ncbi.nlm.nih.gov/pubmed/24587271http://www.pubmedcentral.nih.gov/articlerender.fcgi?artid=PMC3937378https://dx.plos.org/10.1371/journal.pone.0090189.

[86] T S Baker, N H Olson, and S D Fuller. "Adding the Third Dimension to Virus Life Cycles: Three-Dimensional Reconstruction of Icosahedral Viruses from Cryo-Electron Micrographs". In: *MICROBIOLOGY AND MOLECULAR BIOLOGY REVIEWS* 63 (4 1999), pp. 862–922.

[87] D. Dasgupta, F. Demichelis, and A. Tagliaferro. "Electrical conductivity of amorphous carbon and amorphous hydrogenated carbon". In: *Philosophical Magazine B* 63 (6 2006), pp. 1255–1266. ISSN: 13642812. DOI: 10.1080/13642819108205558. URL: https://www.tandfonline.com/doi/abs/10.1080/13642819108205558.

[88] Vinson Lam and Elizabeth Villa. "Practical approaches for cryo-FIB milling and applications for cellular cryo-electron tomography". In: *Methods in molecular biology (Clifton, N.J.)* 2215 (2021), p. 49. ISSN: 19406029. DOI: 10.1007/978-1-0716-0966-8_3.

URL: /pmc/articles/PMC8836527//pmc/articles/PMC8836527/?report=abstracthttps://www.ncbi.nlm.nih.gov/pmc/articles/PMC8836527/.

[89]    Antti Peltonen et al. "Milling a silicon nitride membrane by focused ion beam". In: *Journal of Vacuum Science  Technology B, Nanotechnology and Microelectronics: Materials, Processing, Measurement, and Phenomena* 34 (6 Nov. 2016), p. 062201. ISSN: 2166-2746. DOI: 10.1116/1.4963895. URL: https://avs.scitation.org/doi/abs/10.1116/1.4963895.

[90]    Ning Wang, James P. Butler, and Donald E. Ingber. "Mechanotransduction Across the Cell Surface and Through the Cytoskeleton". In: *Science* 260 (5111 1993), pp. 1124–1127. ISSN: 00368075. DOI: 10.1126/SCIENCE.7684161. URL: https://www.science.org/doi/10.1126/science.7684161.

[91]    Peter Meinke and Eric C. Schirmer. "LINC'ing form and function at the nuclear envelope". In: *FEBS Letters* 589 (19PartA Sept. 2015), pp. 2514–2521. ISSN: 00145793. DOI: 10.1016/j.febslet.2015.06.011. URL: http://www.ncbi.nlm.nih.gov/pubmed/26096784http://doi.wiley.com/10.1016/j.febslet.2015.06.011.

[92]    Meredith H. Wilson and Erika L.F. Holzbaur. "Nesprins anchor kinesin-1 motors to the nucleus to drive nuclear distribution in muscle cells". In: *Development* 142 (1 Jan. 2015), pp. 218–228. ISSN: 0950-1991. DOI: 10.1242/DEV.114769. URL: https://journals.biologists.com/dev/article/142/1/218/46986/Nesprins-anchor-kinesin-1-motors-to-the-nucleus-to.

[93]    Georgia Salpingidou et al. "A novel role for the nuclear membrane protein emerin in association of the centrosome to the outer nuclear membrane". In: *Journal of Cell Biology* 178 (6 Sept. 2007), pp. 897–904. ISSN: 0021-9525. DOI: 10.1083/JCB.200702026. URL: http://www.jcb.org/cgi/doi/10.1083/jcb.200702026.

[94]    Alexandre Ottaviani et al. "Identification of a perinuclear positioning element in human subtelomeres that requires A-type lamins and CTCF". In: *The EMBO Journal* 28 (16 Aug. 2009), pp. 2428–2436. ISSN: 1460-2075. DOI: 10.1038/EMBOJ.2009.201. URL: https://onlinelibrary.wiley.com/doi/full/10.1038/emboj.2009.201https://onlinelibrary.wiley.com/doi/abs/10.1038/emboj.2009.201https://www.embopress.org/doi/abs/10.1038/emboj.2009.201.

[95]    Alexandre Mejat and Tom Misteli. "LINC complexes in health and disease". In: *Nucleus* 1 (1 2010), pp. 40–52. ISSN: 19491042. DOI: 10.4161/NUCL.1.1.10530. URL: https://www.tandfonline.com/doi/abs/10.4161/nucl.1.1.10530.

[96]    Pascale Schellenberger et al. "High-precision correlative fluorescence and electron cryo microscopy using two independent alignment markers". In: *Ultramicroscopy* 143 (100 2014), pp. 41–51. ISSN: 1879-2723. DOI: 10.1016/J.ULTRAMIC.2013.10.011. URL: https://pubmed.ncbi.nlm.nih.gov/24262358/.

[97]   Georg Wolff et al. "Towards correlative super-resolution fluorescence and electron cryo-microscopy". In: *Biology of the cell* 108 (9 Sept. 2016), p. 245. ISSN: 1768322X. DOI: 10.1111/BOC.201600008. URL: /pmc/articles/PMC5524168//pmc/articles/PMC5524168/?report=abstracthttps://www.ncbi.nlm.nih.gov/pmc/articles/PMC5524168/.

[98]   Wakam Chang et al. "Linker of nucleoskeleton and cytoskeleton (LINC) complex-mediated actin-dependent nuclear positioning orients centrosomes in migrating my-oblasts". In: *Nucleus* 6 (1 Jan. 2015), pp. 77–88. ISSN: 1949-1034. DOI: 10.1080/19491034.2015.1004947. URL: http://www.ncbi.nlm.nih.gov/pubmed/25587885http://www.pubmedcentral.nih.gov/articlerender.fcgi?artid=PMC4615731http://www.tandfonline.com/doi/full/10.1080/19491034.2015.1004947.

[99]   Ruijun Zhu, Susumu Antoku, and Gregg G. Gundersen. "Centrifugal Displacement of Nuclei Reveals Multiple LINC Complex Mechanisms for Homeostatic Nuclear Posi-tioning". In: *Current Biology* 27 (20 Oct. 2017), 3097–3110.e5. ISSN: 09609822. DOI: 10.1016/J.CUB.2017.08.073.

[100]  D Studer et al. *A new approach for cryofixation by high-pressure freezing*. 2001, pp. 285–294. URL: http://www.ana.unibe.ch/empact.

[101]  Daniel Studer, Bruno M. Humbel, and Matthias Chiquet. "Electron microscopy of high pressure frozen samples: Bridging the gap between cellular ultrastructure and atomic resolution". In: *Histochemistry and Cell Biology* 130 (5 Nov. 2008), pp. 877–889. ISSN: 09486143. DOI: 10.1007/S00418-008-0500-1/FIGURES/5. URL: https://link.springer.com/article/10.1007/s00418-008-0500-1.

[102]  Kent L. McDonald and Manfred Auer. "High-pressure freezing, cellular tomography, and structural cell biology". In: *BioTechniques* 41 (2 May 2006), pp. 137–143. ISSN: 07366205. DOI: 10.2144/000112226/ASSET/IMAGES/LARGE/FIGURE2.JPEG. URL: https://www.future-science.com/doi/10.2144/000112226.

[103]  Marie Versaevel et al. "Super-resolution microscopy reveals LINC complex recruitment at nuclear indentation sites". In: (2014). DOI: 10.1038/srep07362. URL: www.nature.com/scientificreports.

[104]  G. W.Gant Luxton et al. "Linear Arrays of Nuclear Envelope Proteins Harness Retrograde Actin Flow for Nuclear Movement". In: *Science (New York, N.Y.)* 329 (5994 Aug. 2010), p. 956. ISSN: 00368075. DOI: 10.1126/SCIENCE.1189072. URL: /pmc/articles/PMC3938394//pmc/articles/PMC3938394/?report=abstracthttps://www.ncbi.nlm.nih.gov/pmc/articles/PMC3938394/.

[105]  David N. Mastronarde. "Automated electron microscope tomography using robust pre-diction of specimen movements". In: *Journal of structural biology* 152 (1 Oct. 2005), pp. 36–51. ISSN: 1047-8477. DOI: 10.1016/J.JSB.2005.07.007. URL: https://pubmed.ncbi.nlm.nih.gov/16182563/.

[106] Mauricio Toro-Nahuelpan et al. "Tailoring cryo-electron microscopy grids by photo-micropatterning for in-cell structural studies". In: *Nature Methods* (2020). DOI: 10.1038/s41592-019-0630-5. URL: https://doi.org/10.1038/s41592-019-0630-5.

[107] Laura M. Hoffman et al. "Mechanical stress triggers nuclear remodeling and the formation of transmembrane actin nuclear lines with associated nuclear pore complexes". In: *Molecular Biology of the Cell* (2020). DOI: 10.1091/mbc.E19-01-0027.